https://doi.org/10.5194/egusphere-2026-6528
Preprint. Discussion started: 9 November 2026
© Author(s) 2026. CC BY 4.0 License.

Atmospheric observations reveal Alaskan wetland CH_4 fluxes are up to threefold higher than process-based model estimates

Hanyu Liu[1], Charles E. Miller[2], Colm Sweeney[3], Kathryn Mckain[3], Jennifer D. Watts[4], Róisín Commane[5,6], Luke D. Schiferl[6], Zhen Zhang[7], Benjamin Poulter[8], Leyang Feng[1], Ao Chen[1], Ziting Huang[1], Dylan C. Gaeta[1], Kristan L. Morgan[1], William S. Daniels[1], Qiulun Li[1], Joe R. Melton[9], Vineet Yadav[2], Deborah Huntzinger[10], and Scot M. Miller[1]

[1]Department of Environmental Health and Engineering, Johns Hopkins University, Baltimore, MD, USA
[2]Jet Propulsion Laboratory, California Institute of Technology, Pasadena, CA, USA
[3]National Oceanic and Atmospheric Administration, Global Monitoring Laboratory, Boulder, CO, USA
[4]Woodwell Climate Research Center, Falmouth, MA, USA
[5]Department of Earth and Environmental Sciences, Columbia University, New York, NY, USA
[6]Lamont-Doherty Earth Observatory, Columbia University, Palisades, NY, USA
[7]Institute of Tibetan Plateau Research, Chinese Academy of Sciences, Beijing, China
[8]Spark Climate Solutions, San Francisco, CA, USA
[9]Environment and Climate Change Canada, Victoria, BC, Canada
[10]School of Earth and Sustainability, Northern Arizona University, Flagstaff, AZ, USA

Correspondence: Hanyu Liu (hliu154@jhu.edu)

Abstract. Amplified Arctic warming could substantially increase methane (CH_4) fluxes from high-latitudes by accelerating soil thaw and releasing soil organic carbon into the atmosphere. Yet, the magnitude and spatiotemporal patterns of current and future high-latitude CH_4 fluxes remain highly uncertain. We estimate growing season (May to September) CH_4 fluxes in Alaska from 2012 to 2017 using atmospheric observations from two NASA campaigns: the Carbon in Arctic Reservoirs Vulnerability Experiment (CARVE) and Arctic-Carbon Atmospheric Profiles (Arctic-CAP). We couple these observations with an atmospheric transport model and a geostatistical inverse model to estimate the geographic distribution, seasonality, and inter-annual variability of CH_4 fluxes. As part of this approach, we evaluate how well different state-of-the-art, process-based flux models compare to the inverse estimate of CH_4 fluxes. We find that estimated statewide fluxes are a factor of 1.3 to 2.9 higher compared to different ensembles of process-based models. This discrepancy is largest across the North Slope of Alaska - up to a factor of 6.5 when compared to one of the model ensembles. We do not find any statistically significant inter-annual variability (IAV) during years 2012 – 2017, and the IAV in our estimate is generally consistent with process-based models. In addition, our analysis reveals that differences in inundation fraction mapping contribute to the magnitude discrepancies in current process-based models, and future improvements in inundation maps are essential to reduce uncertainties in CH_4 flux estimates across high latitudes. These results provide an improved atmospheric constraint on regional CH_4 flux estimates from northern wetlands under accelerated Arctic warming.

https://doi.org/10.5194/egusphere-2026-6528
Preprint. Discussion started: 9 November 2026
© Author(s) 2026. CC BY 4.0 License.

1 Introduction

During the past 50 years, the Arctic has warmed three to four times faster than the global mean, and studies have estimated that $\sim 70-100\,\%$ of the near-surface permafrost will be lost by 2100 (e.g., Guo et al., 2025; Schaefer et al., 2011; Peng et al., 2023; Rantanen et al., 2022; Li et al., 2023). Within these northern permafrost regions, the total soil organic carbon (SOC) reservoir is estimated to store 1140 to 1476 peta-grams (Pg C) of carbon, which is 100 times higher than annual global carbon fluxes from fossil fuels in 2024 (Hugelius et al., 2014; Friedlingstein et al., 2025). As carbon-rich permafrost thaws, previously frozen SOC is exposed to microbial decomposition under oxygen-limited conditions, regardless of whether the soil is fully inundated. These oxygen-limited conditions support the final stage of anaerobic decomposition (methanogenesis), where methanogenic archaea produce CH_4 from substrates such as acetate, carbon dioxide (CO_2), and hydrogen, as well as methylated compounds. Based on recent Arctic CH_4 flux studies, CH_4 flux estimates from Pan-Arctic wetlands and inland waters have increased by approximately 30 % since 2000, and future projections suggest that total global CH_4 fluxes will increase by more than 100 % by 2100 (e.g., Liu and Zhuang, 2023a; Rößger et al., 2022; Yuan et al., 2024; Tan and Zhuang, 2015). As permafrost continues to thaw with rising temperatures, studies disagree on whether Arctic ecosystems are net carbon sources or sinks based on net ecosystem exchange, but these assessments do not always include CH_4 fluxes, which may increase the overall warming impact in the Arctic region (e.g., Fisher et al., 2014; Commane et al., 2017; MacGilchrist et al., 2014).

Process-based (bottom-up) models are widely used to estimate both current and projected future wetland CH_4 fluxes (e.g., Wania et al., 2013; Zhuang et al., 2023; Liu et al., 2026; Ito and Inatomi, 2012). These models differ in how they represent wetland area. Some models simulate changes in inundation fractions per grid cell using their own hydrological calculations, whereas others use prescribed inundation fraction maps derived from external datasets, such as remote-sensing products (Zhang et al., 2025). These estimates determine where and over what area wetland CH_4 fluxes occur. The models then use environmental drivers such as soil carbon to calculate the amount of CH_4 fluxes emitted from that area. Differences in both inundation fraction maps and model processes can therefore affect the magnitude and spatial-temporal patterns of the process-based CH_4 flux estimates. The Wetland and Wetland CH_4 Intercomparison of Models Project (WETCHIMP) is a multi-model comparison project from 2013 designed to evaluate an earlier generation of global process-based wetland CH_4 flux models (e.g., Wania et al., 2013; Melton et al., 2013). Since WETCHIMP, more recent generations of global process-based CH_4 models have been developed and are now included as part of the Global Carbon Project (GCP) CH_4 budget assessments. These process-based models have shown large uncertainties in both global and regional CH_4 flux estimates. For example, Saunois et al. (2025) report that the global wetland CH_4 fluxes range from 131 to 198 Tg CH_4 per year. Within high-latitude regions (60°–90° N), these wetland flux estimates range from 9 to 53 Tg CH_4 per year. At a regional scale in Alaska, CH_4 fluxes estimated by WETCHIMP models range from 0.5 to 7 Tg CH_4 per year, while the flux estimates for the most recent GCP model ensembles produce a narrower range of 0.3 to 3.6 Tg CH_4 per year for the same region (Chang et al., 2014a; Liu et al., 2026; Fisher et al., 2014). The GCP models have a smaller inter-model spread than the earlier WETCHIMP models across Canada and Alaska, but better inter-model agreement does not necessarily guarantee that the models are more accurate (e.g., Liu et al., 2026).

https://doi.org/10.5194/egusphere-2026-6528
Preprint. Discussion started: 9 November 2026
© Author(s) 2026. CC BY 4.0 License.

A complementary approach to evaluate process-based models is to use top-down inverse modeling. Instead of relying on prescribed biogeochemical processes, inverse models integrate atmospheric observations with an atmospheric transport model to infer regional CH_4 fluxes (e.g., Miller et al., 2016c, a; Chang et al., 2014b). Satellite retrievals such as Greenhouse gas Observing Satellite (GOSAT) and the Tropospheric Monitoring Instrument (TROPOMI) provide extensive spatial coverage of CH_4 observations, and existing satellite-based CH_4 inverse modeling studies have shown that the estimated global CH_4 fluxes from all natural sources are within the range of 193 to 241 Tg CH_4 per year based on Saunois et al. (2025). However, these satellite data face challenges in capturing accurate CH_4 mixing ratios in high-latitude regions due to low solar angles, high cloud cover, and polar night (e.g., Ward et al., 2025; Wittig et al., 2023; Gao et al., 2023; Watts et al., 2026). Other top-down studies have used atmospheric CH_4 measurements from in situ tower networks to quantify the magnitude and spatiotemporal variability of high-latitude North American CH_4 fluxes (e.g., Worthy et al., 1998; Miller et al., 2014; Pickett-Heaps et al., 2011; Ishizawa et al., 2024; Fujita et al., 2018; Thompson et al., 2017). These studies report that total Canadian CH_4 fluxes from all sources range from 14.8 to 19.5 Tg CH_4 per year, with fluxes from the Hudson Bay Lowlands (HBL) ranging from 1.56 to 3.4 Tg CH_4 per year. These flux totals are much lower than those estimated by most of the WETCHIMP and GCP process-based models (e.g., Liu et al., 2026; Miller et al., 2014, 2016a). By contrast, existing inverse modeling studies argue that fluxes from Alaska are generally higher than those from the WETCHIMP models (e.g., Miller et al., 2016c; Hartery et al., 2018; Chang et al., 2014a). However, these studies have not analyzed the much newer ensemble of GCP models across Alaska.

Historically, Canada has had an extensive atmospheric tower-based observing network, but Alaska does not. It is difficult to constrain atmospheric CH_4 in regions where tower-based observations are sparse and satellite retrievals perform poorly. As a result, National Aeronautics and Space Administration (NASA) launched two intensive airborne measurement campaigns in Alaska and parts of northwest Canada: the Carbon in Arctic Reservoirs Vulnerability Experiment (CARVE) and Arctic Carbon Aircraft Profile (Arctic-CAP) (conducted as part of the Arctic-Boreal Vulnerability Experiment (ABoVE)). Atmospheric inverse modeling studies have used CH_4 observations from the CARVE and Arctic-CAP aircraft campaigns to estimate Alaskan CH_4 fluxes in Alaska, providing a range of estimates of 1.5 to 2.9 Tg CH_4 per year (e.g., Miller et al., 2016c; Chang et al., 2014a; Hartery et al., 2018; Sweeney et al., 2022). Existing studies also report that most bottom-up models underestimate CH_4 fluxes from Alaska's North Slope (e.g., Chang et al., 2014a; Miller et al., 2016c; Sweeney et al., 2022; Hartery et al., 2018; Zona et al., 2016). Existing atmospheric inverse modeling studies of Alaska, however, either rely on a single year or at most three of the five years of intensive aircraft measurements from the CARVE and Arctic-CAP campaign data(e.g., Chang et al., 2014a; Miller et al., 2016c; Hartery et al., 2018).

In this study, we integrate five years (2012-2015, and 2017) of intensive aircraft measurements from CARVE and Arctic-CAP campaigns with an atmospheric transport model and a geostatistical inverse model (GIM) to quantify CH_4 fluxes in Alaska. We can compare how process-based model estimates have evolved over time and whether these newer models are more consistent with atmospheric observations compared to earlier models. As part of this study, we first analyze the magnitude and spatial distribution of the estimated CH_4 fluxes based on our inverse model and the process-based GCP models in Alaska. Second, we compare the inter-annual variability (IAV) of our estimated fluxes with those from the GCP and WETCHIMP models. Third, we explore the seasonal cycle in our posterior estimate and process-based flux estimates. Finally, we identify which

https://doi.org/10.5194/egusphere-2026-6528
Preprint. Discussion started: 9 November 2026
© Author(s) 2026. CC BY 4.0 License.

environmental drivers (e.g., soil moisture, soil carbon, soil temperature) can best explain the spatiotemporal patterns of CH_4 fluxes in Alaska. This analysis provides insights that may help guide future improvements to regional wetland CH_4 estimates in global, process-based flux models.

2 Data and methods

2.1 CARVE and Arctic-CAP aircraft CH_4 measurements

In this study, we use continuous, in situ aircraft CH_4 observations collected during two intensive NASA aircraft campaigns: CARVE and Arctic-CAP (Sweeney et al., 2016b, 2019; Chang et al., 2014a; Sweeney et al., 2022). CARVE provides in situ atmospheric measurements for CH_4, CO_2, CO, and H_2O in Alaska between March and November during years 2012-2015. The CARVE campaign features repeated vertical profiles along each flight track with five-second intervals between observations. The CARVE campaign data span from 58° N to 72° N and 168° W to 131° W, covering most of Alaska and some parts of the Yukon and Northwest Territories in Canada (Figure 1). Two Picarro cavity ring-down spectrometers were used by teams from the National Oceanic and Atmospheric Administration (NOAA) and Harvard University to analyze in situ measurements on the C-23 Sherpa aircraft. However, the in situ aircraft measurements collected and analyzed by Harvard University ended after 2014, so we only focus on NOAA's CH_4 observations that span the entire 2012–2015 analysis period.

We also use data from the Arctic-CAP campaign, which spans from April to November in 2017, ranging from 58° N to 71° N and 165° W to 112° W (Sweeney et al., 2019). The Arctic-CAP campaign includes continuous in situ atmospheric measurements of CH_4 and CO_2 collected using a Picarro G2401 over Alaska, with some measurements over the Yukon and Northwest Territories. These flights include over 25 vertical profiles from the surface up to 6000 meters in altitude each month (Sweeney et al., 2019, 2022). These trace gas measurements collected from both campaigns have data availability about 7 to 10 days per month during the collection period. Together, these aircraft campaigns provide a five-year record of atmospheric CH_4 measurements with extensive spatial coverage over Alaska, offering valuable constraints on CH_4 fluxes.

2.2 Wetland CH_4 flux model ensembles: GCP and WETCHIMP

There are ten global process-based models included in the WETCHIMP, but only seven provide complete spatial coverage for Alaska (e.g., Melton et al., 2013; Wania et al., 2013; Bohn et al., 2015; Miller et al., 2016a). These models include SDGVM (Singarayer et al., 2011), ORCHIDEE (Riley et al., 2011), LPJ-WSL (Hodson et al., 2011), LPJ-Bern (Zürcher et al., 2013), LPJ-WhyMe (Wania et al., 2010), DLEM (Tian et al., 2010), and CLM4Me (Riley et al., 2011). A general description of the WETCHIMP models is given in Table 2 of Wania et al. (2013). The WETCHIMP project provides monthly CH_4 flux estimates for years from 1993 through 2004. Across the ensemble, three general approaches are used to define wetland areal extent: (1) prescribe a static inundation fraction estimate (LPJ-WhyMe and LPJ-Bern), (2) use a remote sensing inundation product such as the Global Inundation Extent from Multi-Satellites (GIEMS) (CLM4Me, DLEM, ORCHIDEE, LPJ-WSL, and LPJ-Bern), or (3) estimate inundation fraction internally based on models' hydrological schemes (SDGVM) (Wania et al., 2013; Melton

https://doi.org/10.5194/egusphere-2026-6528
Preprint. Discussion started: 9 November 2026
© Author(s) 2026. CC BY 4.0 License.

et al., 2013). The WETCHIMP model outputs have native spatial resolutions that range from 0.5° latitude by 0.5° longitude to 2.5° latitude by 1.9° longitude, and we regrid the model outputs into a uniform spatial resolution of 0.5° latitude by 0.5° longitude using the Climate Data Operators (CDO) software (Schulzweida, 2023).

We also evaluate 16 global process-based wetland CH_4 flux models from the GCP that span the years 2000 to 2020 (Zhang et al., 2025). Detailed descriptions of these models are provided in Table S2 of Liu et al. (2026) and Table S1 of Zhang et al. (2025). The GCP ensemble includes two types of simulations – prognostic and diagnostic. The prognostic simulations (available for 11 of the 16 models) use inundation fraction maps that are generated internally using each model's biogeochemical schemes (Zhang et al., 2025). In contrast, the diagnostic simulations (available for all 16 models) use a common prescribed inundation fraction: the Wetland Area and Dynamics for Methane Modeling version 2 (WAD2Mv2), which is a global monthly wetland-fraction product from 2000–2020 with a spatial resolution of $0.25°$ latitude by $0.25°$ longitude (Zhang et al., 2021a). The diagnostic simulations of the GCP models therefore isolate the differences in model process representations by eliminating inter-model differences in inundation fraction maps. Note that previous studies have shown that the inundated area estimated by WAD2M v2 has substantial uncertainty, including challenges such as double-counting of inland freshwater, inclusion of non-inundated wetlands, and larger wetland fractions over peatland regions compared with other products such as the TOPography-based hydrological MODEL (TOPMODEL) (e.g., Kyzivat and Smith, 2023; Bernard et al., 2025b; Zhang et al., 2025). Unlike the WETCHIMP models, there are two sets of GCP model simulations that are driven by two different meteorological products, including a monthly ground-based climate forcing data product from Climate Research Unit 4.06 (CRU) and a daily climate forcing data product from the Global Soil Wetness Project Phase 3 (GSWP3-W5E5) (Harris et al., 2022; Cucchi et al., 2020; Dirmeyer et al., 2006; Lange et al., 2021; Kim, 2017). Ito et al. (2023) and Zhang et al. (2025) report that the flux differences between GCP models driven by different climate forcing datasets are minimal. In this study, we only work with 11 prognostic and 16 diagnostic GCP model simulations driven by CRU climate data. Similarly, we re-grid the GCP models to a uniform spatial resolution of 0.5° latitude by 0.5° longitude using the CDO software (Schulzweida, 2023).

2.3 Atmospheric modeling

We link the estimated surface fluxes from the GCP models with aircraft CH_4 observations from CARVE and Arctic-CAP using the Weather Research and Forecasting-Stochastic Time-Inverted Lagrangian Transport model (WRF-STILT), which is a widely used meteorology-driven trace gas transport model (e.g., Lin et al., 2003; Zhao et al., 2009; Skamarock and Klemp, 2008; McKain et al., 2015; Feng et al., 2023; Miller et al., 2013, 2016c; Jeong et al., 2012; Schiferl et al., 2022). We use WRF-STILT model simulations generated for each individual CARVE and Arctic-CAP measurement. For each of these observations, the STILT transport model releases a cluster of tracer particles and follows them backward in time (in this case, for 10 days) following the wind fields in the WRF model. This model provides a sensitivity field (or the "footprint" map) shown in Fig. 1, which represents the sensitivity of each aircraft observation to a unit surface CH_4 flux across different upwind locations and time steps (Henderson et al., 2017, 2021). Note that footprints do not include any information about surface fluxes or emissions inventories; instead, they are multiplied by a gridded flux estimate to calculate the modeled CH_4 mixing ratio enhancement

https://doi.org/10.5194/egusphere-2026-6528
Preprint. Discussion started: 9 November 2026
© Author(s) 2026. CC BY 4.0 License.

corresponding to each aircraft measurement. Here, we define the enhancement as the change in the CH_4 mixing ratio caused by fluxes that occur within the study domain (see the paragraphs below in this section).

The WRF simulations used in our study were specifically designed for STILT simulations at high latitudes using the polar variant of the WRF model (Henderson et al., 2015). The footprint fields have units of ppb per unit surface flux (μmol m^{-2} s^{-1}) and originally cover the spatial domain of 30°S to 90°N and 180°W to 180°E with a spatial resolution of 0.5° latitude by 0.5° longitude. When multiplying the STILT footprints by the GCP flux estimates, we retain the full subdomain (50°N to 75°N and 180°W to 100°W) to avoid accidentally removing regions that may have some influence on the CH_4 observations near the Alaskan boundaries. However, we focus on the results for Alaska where most of the aircraft observations were collected.

We multiply anthropogenic, biomass burning, and natural CH_4 flux estimates by the WRF-STILT footprints to compute the total modeled mixing ratios. For anthropogenic fluxes, we use year-specific EDGAR v6.0 from Crippa et al. (2026), which is a global CH_4 inventory with annual temporal resolution and a spatial resolution of 0.1° latitude by 0.1° longitude. For fire fluxes, we use Global Fire fluxes Database, Version 5.1 (GFEDv5) from van der Werf et al. (2025), which includes year-specific daily estimates of global burned areas with an original spatial resolution of 0.25° latitude by 0.25° longitude. For other non-wetland natural sources, we use the static, non-year-specific geological seep flux map from Etiope et al. (2019). In this study, we do not include a separate lake CH_4 flux product because doing so may double-count CH_4 fluxes that are already represented in the GCP wetland models (e.g., Thornton et al., 2016). Several recent studies have shown that inundation products can implicitly include portions of lakes, leading to potential overlap between lake and wetland fluxes (Kyzivat and Smith, 2023; Melack and Hess, 2023; Liu and Zhuang, 2023b; Grasset et al., 2025).

We filter for all aircraft CH_4 measurements collected above 2000 meters above ground level (agl) and use the daily mean as the boundary conditions for each observation, which is the same approach described by Miller et al. (2016c). In this case, boundary conditions refer to the clean background CH_4 transported into our study domain from other regions of the world. Air masses above 2000 meters generally lie above both the planetary boundary layer and the residual layer. As a result, these high-altitude measurements are treated as free-tropospheric mixing ratios that can be used to represent the regional background for that day. Miller et al. (2016c) tested an alternative boundary-condition estimate derived from aircraft measurements at 3000 meters agl and found that the mean growing-season (May–October) CH_4 flux estimate, averaged over 2012 to 2014, changed by only 1.1%.

After we multiply the GCP flux models and each of the additional sector-specific CH_4 flux products with WRF-STILT footprints, we sum these products and the boundary conditions to calculate the total modeled mixing ratios. These modeled mixing ratios ($\hat{\boldsymbol{z}}$, dimensions $n \times 1$, where n represents the total number of observations) are directly comparable to atmospheric CH_4 observations ($\boldsymbol{z}$) collected during the CARVE and Arctic–CAP campaigns. We specifically model atmospheric CH_4 ($\hat{\boldsymbol{z}}$) using the following equation (e.g., Fang and Michalak, 2015):

$$\hat{\boldsymbol{z}} = \mathbf{H}(\boldsymbol{W} + \boldsymbol{A} + \boldsymbol{N} + \boldsymbol{B}) + \boldsymbol{b}. \quad (1)$$

https://doi.org/10.5194/egusphere-2026-6528
Preprint. Discussion started: 9 November 2026
© Author(s) 2026. CC BY 4.0 License.

This equation shows the model estimate at the observation locations ($\hat{\boldsymbol{z}}$), calculated using (1) the boundary condition ($\boldsymbol{b}$, dimensions $n \times 1$) and (2) the product of the footprints and the combined surface flux estimates. The footprints generated from WRF-STILT are represented by $\mathbf{H}$ with dimensions of $n \times m$, where m represents the total number of model grid boxes in space and time.

The combined surface flux estimates include process-based model estimates from the GCP ($\boldsymbol{W}$, dimensions of $m \times 1$), anthropogenic CH_4 flux estimates from EDGAR v6.0 ($\boldsymbol{A}$, dimensions of $m \times 1$), geological seep and termite CH_4 flux estimates from Fung et al. (1991) and Etiope et al. (2019) ($\boldsymbol{N}$, dimensions of $m \times 1$), and biomass burning estimates from GFEDv5 ($\boldsymbol{B}$, dimensions of $m \times 1$). After calculating this equation, we can subsequently compare our model estimates ($\hat{\boldsymbol{z}}$) directly with $\boldsymbol{z}$.

Note that CH_4 has an atmospheric lifetime of about 10 years and is gradually removed by oxidation with hydroxyl radicals (OH). Our STILT setup does not include OH chemistry, but the omission likely has a negligible impact on our results. STILT footprints show the highest sensitivities within the first two days upwind of each observation, and the loss of CH_4 on such short time scales is very small (usually less than 2 ppb) (Miller et al., 2013).

2.4 Geostatistical Inverse Model (GIM)

We use a geostatistical inverse model (GIM) to estimate surface CH_4 fluxes that best explain the observed CH_4 mixing ratios while accounting for observational and model uncertainties. Many existing studies have used this approach to estimate surface trace gas fluxes (e.g., Miller et al., 2013, 2016c; Fang and Michalak, 2015; Gourdji et al., 2012; Gaeta et al., 2024; Michalak et al., 2004). Unlike traditional inverse models, a GIM does not require an inventory or bottom-up flux model as input to the prior model. Instead, we use model or reanalysis estimates of environmental variables to help capture the spatial and temporal structure of estimated surface CH_4 fluxes (e.g., estimates of temperature and soil moisture). In this study, we refer to these variables as environmental drivers.

2.4.1 Components of the GIM

The inputs to our GIM are atmospheric observations ($\boldsymbol{z}$), boundary conditions ($\boldsymbol{b}$), WRF-STILT footprints ($\mathbf{H}$), and environmental drivers. The output is an estimate of the surface CH_4 fluxes, referred to as the posterior fluxes and estimates of their uncertainties. The posterior fluxes in our GIM are defined by two separate components: the deterministic component and the stochastic component. The deterministic component represents the CH_4 fluxes that we estimate using a combination of environmental drivers such as soil moisture and temperature. These drivers are typically insufficient to explain the full spatial and temporal variability of the true CH_4 fluxes, and these shortfalls arise for several reasons. First, some of the environmental drivers we use are from models or meteorology reanalysis products and may have deficiencies in some locations; some locations may be wetter/drier or warmer/colder than estimated in the Modern-Era Retrospective analysis for Research and Applications, Version 2 (MERRA-2) (Gelaro et al., 2017). Second, the relationships between fluxes and the environmental drivers can be complicated, non-linear, and not fully captured by a linear deterministic model. Third, there may be complex processes that influence CH_4 fluxes that are not included in the deterministic model. In these situations, the stochastic component acts as a correction term, represented by $\boldsymbol{\xi}$ (dimensions $m \times 1$). As part of the inverse model, we estimate values for $\boldsymbol{\xi}$ that can vary

https://doi.org/10.5194/egusphere-2026-6528
Preprint. Discussion started: 9 November 2026
© Author(s) 2026. CC BY 4.0 License.

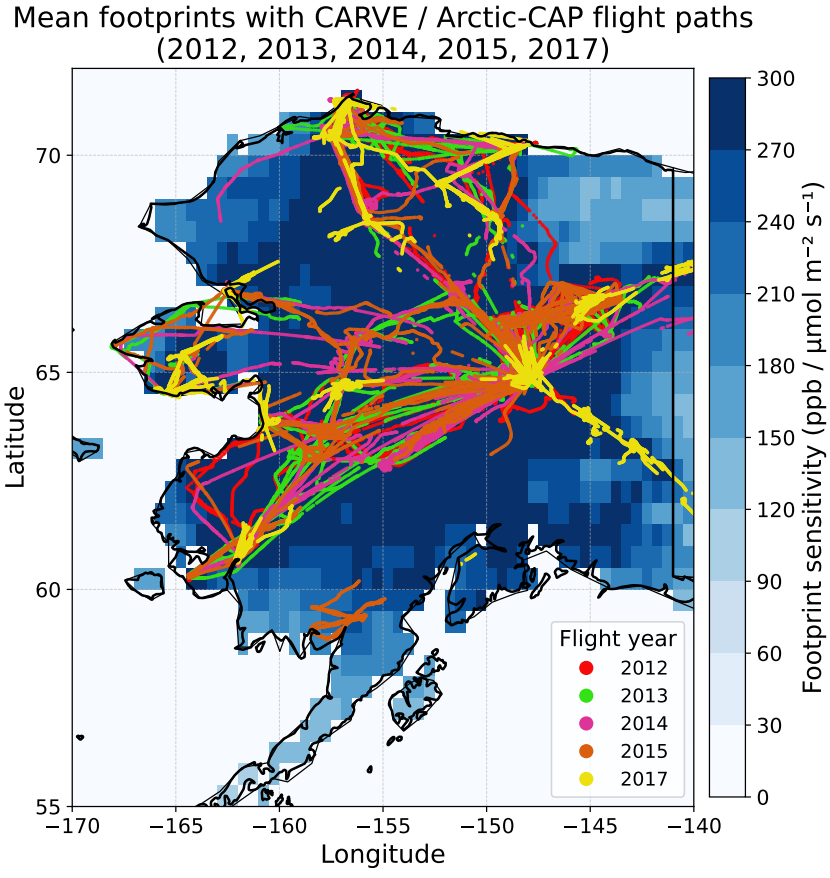


Figure 1. The mean footprints (**H**) estimated for the CARVE and Arctic-CAP aircraft campaigns conducted from 2012 to 2015 and 2017 in Alaska. The colored lines show the aircraft flight paths of CARVE and Arctic-CAP campaigns in each year, restricted to observations at or below 1,500 m above ground level.

among each individual model grid box and on each day of the study period. The stochastic component is thus used to represent the remaining variability in fluxes that cannot be explained by the deterministic model. This structure can be explained by the equation (e.g., Miller et al., 2020; Michalak et al., 2004; Fang and Michalak, 2015):

$$\boldsymbol{s} = \mathbf{X}\boldsymbol{\beta} + \boldsymbol{\xi}. \tag{2}$$

where $\boldsymbol{s}$ denotes the estimated fluxes with dimensions $m \times 1$. $\mathbf{X}$ is an $m \times p$ matrix where each column p corresponds to an environmental driver. $\boldsymbol{\beta}$ shows the corresponding coefficients that we estimated as part of the inverse model, which determine the contribution of each environmental driver to the estimated fluxes (dimensions of $p \times 1$).

https://doi.org/10.5194/egusphere-2026-6528
Preprint. Discussion started: 9 November 2026
© Author(s) 2026. CC BY 4.0 License.

The deterministic component is represented by the term $\mathbf{X}\boldsymbol{\beta}$, and $\boldsymbol{\xi}$ represents the stochastic component of our GIM (each dimension $m \times 1$). The stochastic term $\boldsymbol{\xi}$ is modeled using a multivariate normal distribution with a spatial and temporal correlation structure. Additional methodological details and supporting equations for the geostatistical inverse model are provided in the Supplement (SI). Further explanations of these terms can also be found in previous studies (e.g., Michalak et al., 2004; Miller et al., 2016c; Gaeta et al., 2024).

We estimate the unknown components in Eq. 2 by minimizing a cost function, as described in the SI and in previous studies (e.g., Michalak et al., 2004; Miller et al., 2016c, 2020; Gaeta et al., 2024). We also quantify the uncertainties in the estimated fluxes using the equations presented in the SI and in prior studies (e.g., Michalak et al., 2004; Miller et al., 2020).

2.4.2 Model selection

We test a wide variety of different possible environmental drivers and select the best ones that are most helpful at explaining the spatial and temporal variability of our estimated CH_4 fluxes. We use numerous environmental drivers from NASA's MERRA-2 product ((Global Modeling and Assimilation Office (GMAO), 2015)): soil temperature variables from multiple depth levels: (1) 0–0.1 m below the surface; (2) 0.1–0.2 m below the surface; (3) 0.2–0.4 m below the surface; (4) 0.4–0.8 m below the surface; (5) 0.8–1.5 m below the surface; and (6) 1.5–10 m below the surface. The surface temperature variables include surface air (2 meters) temperatures, surface temperature of land including snow, surface temperature of snow, surface temperature of the saturated zone, surface temperature of the unsaturated zone, a calculated Q_{10} function based on surface temperature of the saturated zone, and a calculated Q_{10} function based on soil temperature (1.5 to 10 m below the surface). The soil moisture and hydrologic variables include surface soil wetness, root zone soil wetness, average profile soil moisture, root zone water, surface layer water, water profile, fractional area of the saturated zone, and fractional area of the unsaturated zone. The freeze–thaw metrics and snow variables include snow depth, land snowfall, and rate of change of total land water. The energy and land-surface water variables include total land precipitation, soil water infiltration rate, overland runoff including throughflow, baseflow flux, and evaporation land flux. In addition, we have also included remote-sensing–based inundation fraction maps from WAD2M v2 (Zhang et al., 2021b); the Kaplan wetland distribution map (Pickett-Heaps et al., 2011; Bergamaschi et al., 2007); a total litter soil carbon pool estimate (Sitch et al., 2003); and the lake fraction dataset from the Global-Gridded Daily Methane Emissions Climatology from Lake Systems, 2003-2015 (Johnson et al., 2022).

We apply a Bayesian Information Criterion (BIC) approach to select a subset of environmental drivers that best captures the spatial and temporal patterns of surface CH_4 fluxes (e.g., Schwarz, 1978; Penny et al., 2007; BIC, 2008; Neath and Cavanaugh, 2012). CH_4 fluxes can be controlled by multiple processes such as soil moisture and temperature, and including more environmental drivers can help us understand which environmental processes best explain the CH_4 signals seen in the atmosphere. At the same time, we want to avoid a model that overfits the available data and fits spurious data errors at the expense of describing true variability in CH_4 fluxes. Overfitting can yield physically unrealistic relationships between the environmental drivers and the fluxes. Model selection using the BIC can prevent the problems of overfitting. The BIC-based model selection approach used in this study has also been adopted in previous GIM studies (e.g., Miller et al., 2016b, 2018; Gourdji et al., 2012). In our study, the estimated BIC score can be written using the equation below (Schwarz, 1978; BIC, 2008):

https://doi.org/10.5194/egusphere-2026-6528
Preprint. Discussion started: 9 November 2026
© Author(s) 2026. CC BY 4.0 License.

$$\mathrm{BIC} = \mathrm{RSS} + p\ln(n), \tag{3}$$

where RSS is the discrepancy (i.e., residual sum of squares) between a proposed deterministic model and the atmospheric CH_4 observations. If RSS is large, then our estimated fluxes, when combined with the WRF-STILT model, are very different from the atmospheric data. $p\ln(n)$ is the penalty term, where p is the number of columns in $\mathbf{X}$ and n is the number of atmospheric observations used in the inverse model. We rank the candidate models according to their BIC scores (BIC) and select the one with the lowest BIC score, and more details on the model selection framework are described in the SI, Schwarz (1978), and Miller et al. (2016c).

Note that we incorporate the environmental drivers into $\mathbf{X}$ in two different ways. In the first approach, we put each different environmental driver in a different column of $\mathbf{X}$, and each variable is assigned a different coefficient by the inverse model ($\boldsymbol{\beta}$). In the second approach, we multiply the different environmental driver variables by one another and include the result as a single column of $\mathbf{X}$. We also tested model combinations both with and without an intercept term in our model selection. In many process-based CH_4 models, the effect of one environmental driver on CH_4 fluxes depends on other drivers. For example, the effect of inundation likely depends on soil temperature. Multiplying the environmental driver variables by one another is a one way to better account for these interactions compared to putting each in a separate column of $\mathbf{X}$.

3 Results and discussion

3.1 Process-based models underestimate fluxes across the North Slope of Alaska

We find that the averaged Alaskan statewide CH_4 flux from 2012 to 2015, and 2017 is 2.0 ± 0.5 Tg CH_4 per growing-season (from May to September), which is a factor of 2.2 greater than the prognostic GCP ensemble mean, 2.9 greater than the diagnostic GCP ensemble mean, and 1.3 greater than the WETCHIMP ensemble mean (Figure 2). Although our GIM does not differentiate among different types of flux sources, existing inventories and process-based models indicate that wetlands are the dominant CH_4 source in high-latitude North America, whereas anthropogenic and non-wetland sources combined contribute an average of 0.2 Tg CH_4 per growing-season from May to September, which is about 9 % of our total posterior estimate (Figure 2). In addition, our finding is consistent with CH_4 flux estimates from previous inverse modeling studies (e.g., Chang et al., 2014a; Hartery et al., 2018; Miller et al., 2016c). Hence, we argue that it is reasonable to compare our estimate of total CH_4 fluxes from Alaska with the wetland-specific GCP and WETCHIMP models. However, the WETCHIMP simulations represent an earlier period than our inverse model study, and some of the differences may reflect temporal changes in environmental conditions and wetland CH_4 fluxes between the two periods.

Our results also show that the GCP model ensemble exhibits a much narrower inter-model spread in its total growing season flux estimates compared to the earlier WETCHIMP models. This reduced inter-model spread from recent GCP models is illustrated by the uncertainty bars shown in Fig. 2, which represent the inter-model spread of the total growing season (May to September) CH_4 fluxes. For each process-based model ensemble and year, we first compute the total growing season flux

https://doi.org/10.5194/egusphere-2026-6528
Preprint. Discussion started: 9 November 2026
© Author(s) 2026. CC BY 4.0 License.

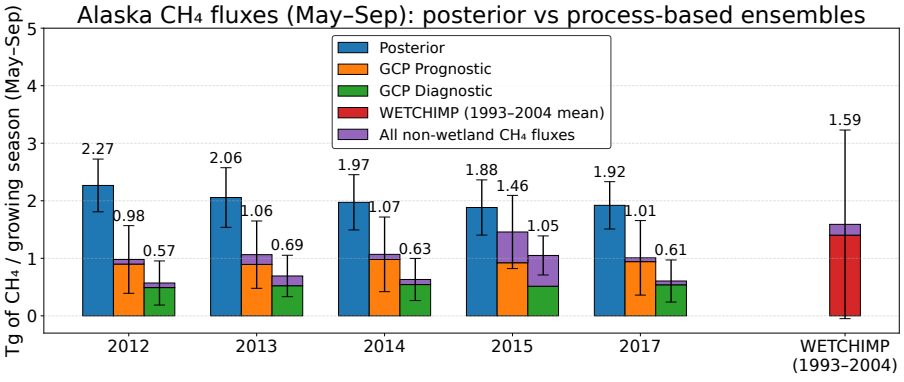


Figure 2. Growing-season (May to September) CH_4 flux totals in Alaska across 2012 to 2015, and 2017. The bars represent each of the flux totals from the posterior estimate (in blue), the prognostic (orange) and diagnostic (green) GCP model ensemble, and the WETCHIMP models (red). Uncertainty bounds for the GCP and WETCHIMP models are calculated as the inter-model spread using ± 1 standard deviation of the total growing season fluxes across all models for each year, and then averaged across years. The stacked purple bars represent the total non-wetland CH_4 fluxes, and these CH_4 flux totals have the unit of Tg CH_4 per growing-season.

for every individual model in the ensemble, and then use the ± 1 standard deviation across those model totals to show the inter-model spread. As shown in Fig. 2, there is a larger spread among the WETCHIMP models compared to the more recent GCP models. This convergence suggests that the modeling community has made efforts toward producing more consistent process-based flux estimates.

However, despite better inter-model agreement, the flux estimates from the GCP models are systematically lower than those from the WETCHIMP models and less consistent with our inverse modeling estimate. Prognostic GCP models produce an average flux of 0.9 ± 0.6 Tg CH_4 per growing season across 2012 to 2015 and 2017. The flux estimates from GCP models with diagnostic runs are even smaller than the prognostic models and our flux estimates, resulting in an average flux of 0.7 ± 0.4 Tg CH_4 per growing season from May to September across the five years of study. By contrast, the flux estimates from WETCHIMP models are averaged over 1993 and 2004, and these flux estimates lie between the posterior flux estimate and GCP model ensembles with a mean of 1.6 ± 1.6 Tg CH_4 per growing season. Note that the non-wetland CH_4 flux totals in 2015 are higher than other years because fire fluxes in 2015 are a factor of 3.5 to 8.3 higher compared to other years (Waigl et al., 2017; Veraverbeke et al., 2017). Although the GCP modeling community has made efforts to reduce inter-model spread, these better inter-model agreement does not necessarily imply better model accuracy (Liu et al., 2026; Chen et al., 2025). In fact, our results suggest that WETCHIMP models may better capture CH_4 fluxes in Alaska compared to more recent GCP models.

We find that the discrepancy between our estimates and the GCP models is greatest across the North Slope, a region that has the most intact or continuous permafrost within Alaska (Jorgenson et al., 2008). Specifically, we find that $\sim 25.4\%$ of Alaska's total CH_4 fluxes come from the North Slope (latitudes $\geq 68°$N). In contrast, 10 out of 11 GCP prognostic models, 15 out of 16 GCP diagnostic models, and all WETCHIMP models simulate proportionally smaller North Slope contributions. Figure 3a shows the spatial distribution of our posterior fluxes, while panels 3c–e present the differences between the posterior

https://doi.org/10.5194/egusphere-2026-6528
Preprint. Discussion started: 9 November 2026
© Author(s) 2026. CC BY 4.0 License.

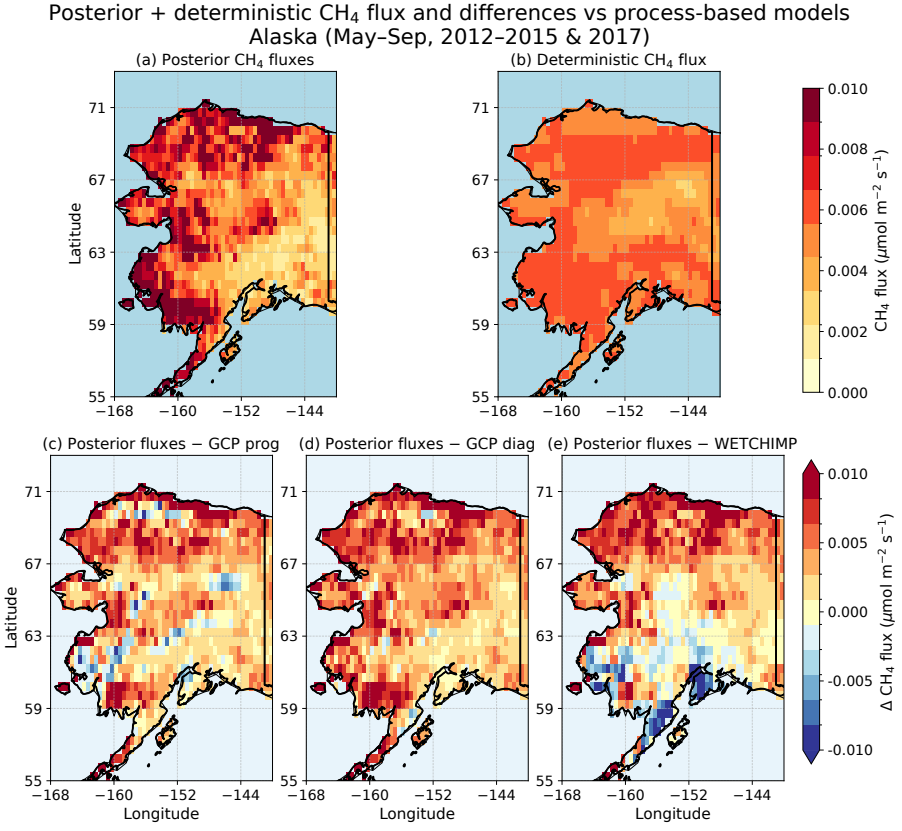


Figure 3. The spatial differences of estimated CH_4 fluxes between posterior estimate versus process-based model ensembles during the growing-seasons in 2012 to 2015, and 2017 in Alaska. Panel (a) represents the posterior flux estimate. Panel (b) represents the deterministic flux estimate. Panel (c) and (d) show the differences between posterior flux estimate and GCP model ensembles ((c) for GCP models with prognostic runs, and (d) for GCP models with diagnostic runs). Panel (e) demonstrates the differences between posterior flux estimate and the WETCHIMP models. All grid-cell values are expressed in units of μmol m^{-2} s^{-1}, and the spatial domain is 55°N to 72°N and 170°W to 140°W.

fluxes and each process-based model ensemble. Specifically, this discrepancy in the North Slope is larger when compared to the WETCHIMP models and improved when compared to the GCP models (e.g., Fisher et al., 2014; Miller et al., 2016c). In the prognostic GCP models, 10.86 % of Alaska's CH_4 fluxes are from the North Slope, whereas that number is 11 % for the diagnostic GCP models and only 3.9 % for the WETCHIMP models (Fig. 4). We further find that Alaska's continuous-permafrost regions account for 31.7 % of the total statewide posterior estimate, which is 61 % greater than the corresponding share in the GCP model ensembles (∼20 %) and about 598 % greater than the corresponding share in the WETCHIMP model ensemble (∼5 %) (Figs. S13 and S14). These results again suggest that the process-based model ensembles allocate too little of Alaska's CH_4 flux on the North Slope of Alaska, a region characterized by continuous permafrost.

https://doi.org/10.5194/egusphere-2026-6528
Preprint. Discussion started: 9 November 2026
© Author(s) 2026. CC BY 4.0 License.

We argue that these differences in the spatial distribution of CH_4 fluxes are likely driven by differences in the underlying inundation estimates. The North Slope accounts for 0.1 % to 38.3 % of Alaska's total fluxes in the prognostic GCP models. For the diagnostic runs, that number spans from 0.5 % to 30.5 %. The largest North Slope CH_4 flux contribution among the GCP estimates is simulated by VISIT (38.3 % for the prognostic version and 30.5 % for the diagnostic version), while its corresponding North Slope share of inundated area is also as high as 39.1 % of the Alaska total. The second-largest simulated contribution is from the JSBACH prognostic model, which yields a North Slope flux share of 23.4 %, with a corresponding inundation share of 28.4 % (Fig. S9). The diagnostic versions of these models yield smaller CH_4 fluxes for the North Slope than their prognostic versions, and the inundation estimate from the diagnostic versions is also lower. In addition, each of these two models uses a different method for inundation, but neither uses remote sensing information like the WAD2M v2 used by the diagnostic GCP models. For example, JSBACH uses TOPMODEL to estimate inundation fractions by combining grid-cell mean water table depth with sub-grid topographic variation (Kleinen et al., 2020). On the other hand, the area over which VISIT simulates CH_4 fluxes from VISIT is prescribed from a static global wetland database constructed by integrating vegetation, soil-property, and fractional-inundation information (Matthews and Fung, 1987). The GCP models use different approaches to estimate inundation, but those that rely on a non-remote-sensing product tend to estimate higher CH_4 fluxes in the North Slope of Alaska for two likely reasons. First, remote-sensing-based surface water products tend to detect surface inundation and may not fully capture saturated soils without visible standing water (e.g., Council, 2014; Ying et al., 2025; Miller et al., 2016c; Liu et al., 2026). Second, these products may underestimate inundation where small ponds or surface water are covered by vegetation, weakening the surface water signal and causing these areas to be classified as non-inundated (e.g., Prigent et al., 2007; Melton et al., 2013; Muster et al., 2013). Together, these limitations may cause remote-sensing-based products to under-represent inundated areas on the North Slope, leading to lower CH_4 flux estimates among the GCP models that use them (e.g., Dong et al., 2024; Bernard et al., 2025a; Marthews et al., 2022; Liu et al., 2026; Lane et al., 2023). To address this problem, radar observations, like the NASA-ISRO synthetic Aperture Radar mission (NISAR), may provide future opportunities to improve the mapping of surface water and inundated vegetation in high-latitude regions (e.g., Rosen et al., 2025). Unlike the coarse satellite observations used in WAD2M v2, NISAR can provide much more detailed radar images that may detect small inundated areas beneath vegetation, helping to improve wetland CH_4 flux estimates from future process-based models. Future higher-resolution radar and microwave radiometer missions could better track near-surface soil moisture and conditions linked to subsurface saturation, improving maps of CH_4-producing wetlands.

We mostly focus on the growing-season Alaskan CH_4 fluxes because we have more consistent aircraft observations during that time. However, observations from October and November also allow us to examine fall shoulder-season CH_4 fluxes in the years when data are available. We estimate a mean fall shoulder-season (Oct-Nov) posterior CH_4 flux estimate of 0.5 Tg of CH_4 across Alaska. This number is equivalent to about 23 % of the mean growing-season posterior CH_4 flux estimate, indicating that non-growing-season CH_4 fluxes are not negligible (Fig. S12). The spatial distribution of these shoulder-season CH_4 fluxes indicates that the North Slope remains an important source region. We estimate that 28 % of the mean fall shoulder-season posterior CH_4 flux estimate comes from the North Slope, which is similar to the 25.4 % North Slope contribution to total Alaska growing-season CH_4 fluxes. This finding is consistent with Zona et al. (2016), which showed that cold-season CH_4

https://doi.org/10.5194/egusphere-2026-6528
Preprint. Discussion started: 9 November 2026
© Author(s) 2026. CC BY 4.0 License.

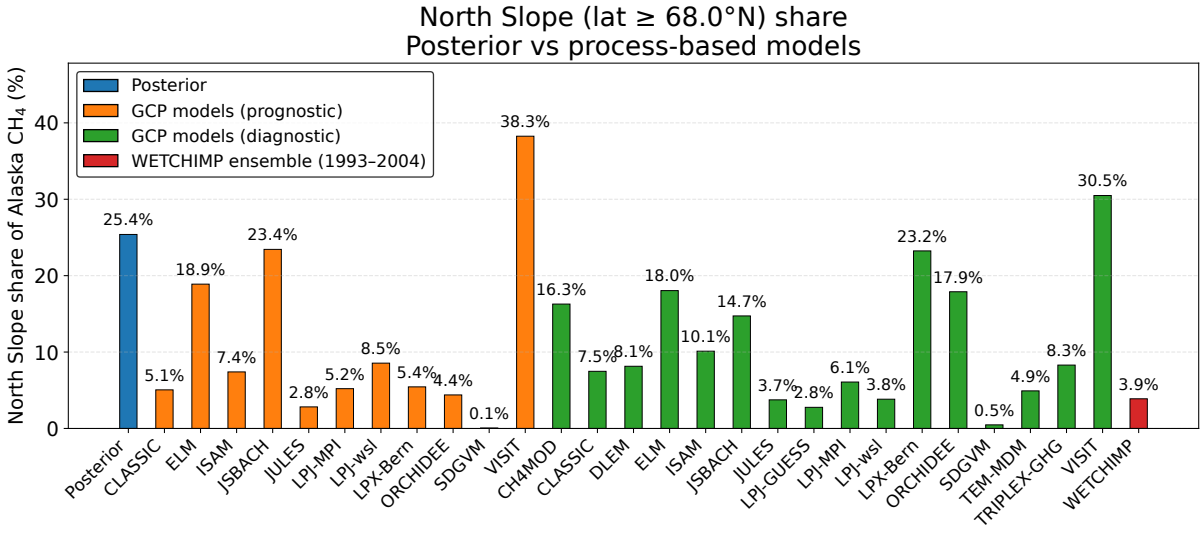


Figure 4. The mean contribution of the North Slope to total Alaska growing-season (May to September) CH_4 flux between our posterior flux estimate and process-based flux estimates from 2012 to 2015, and 2017. Here we define the North Slope as the region of Alaska at a latitude larger or equal to 68°N.

fluxes can make up a large fraction of the Arctic tundra CH_4 budget, with substantial fluxes occurring outside the traditional growing season.

3.2 No evidence of statistically significant inter-annual variability

Our posterior estimate shows some year-to-year variability, but the differences between years are smaller than the uncertainty bounds (± 0.5 Tg CH_4 per growing-season (from May to September)), meaning that we cannot confidently identify statistically significant IAV in the estimated fluxes (Figure 2). Our result on IAV is consistent with some previous inverse modeling studies (Miller et al., 2016c; Sweeney et al., 2016a; Hartery et al., 2018), but differs from other inverse modeling studies that reported stronger IAV or a long-term trend (Thompson et al., 2017; Ward et al., 2024; Ishizawa et al., 2024). To calculate IAV for both our posterior estimate and each process-based model ensemble, we calculate the difference between the monthly averaged maximum and minimum annual growing season flux divided by the monthly averaged mean annual growing season flux. Because WETCHIMP models do not overlap in time with our posterior estimate, we calculate the IAV of WETCHIMP models by repeatedly sampling 5-year periods from all available years, computing IAV for each sample, and averaging the results. In Fig. 5, orange bars correspond to the prognostic GCP model ensemble, green bars to the diagnostic GCP model ensemble, the red bar represents WETCHIMP models (1993–2004), and the blue bar represents our posterior estimate. A caveat of this result is that it is based on five years of observations, and our ability to quantify IAV might be improved with a longer record of observations.

https://doi.org/10.5194/egusphere-2026-6528
Preprint. Discussion started: 9 November 2026
© Author(s) 2026. CC BY 4.0 License.

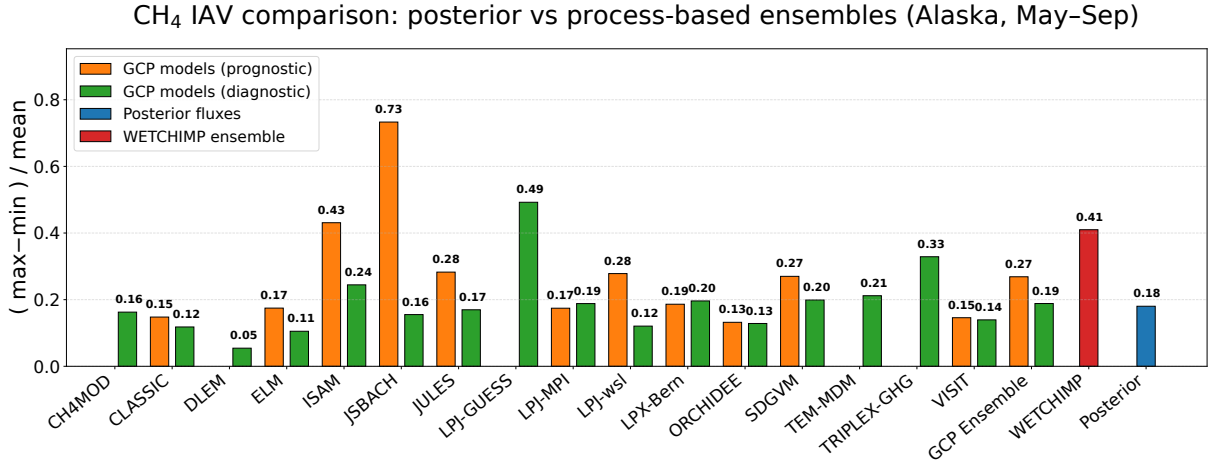


Figure 5. The inter-annual variability (IAV) of CH_4 fluxes from the posterior estimate and from each process-based model ensemble. The IAV values are shown on the y-axis and are calculated using the maximum annual mean monthly fluxes minus the minimum annual mean monthly fluxes, and divide by the mean annual mean monthly fluxes. For WETCHIMP models that span a longer period than GCP models, we estimate the IAV by repeatedly sampling 5-year subsets and averaging across multiple subsets.

Overall, the IAV for our posterior estimate is 18 % during the growing-season from May to September, which is almost identical to the average IAV across the GCP diagnostic model ensemble (19 %) and lower than the averages of the GCP prognostic model ensemble (27 %) and the WETCHIMP model ensemble (41 %). Compared with earlier WETCHIMP models, GCP models have improved inter-model agreement in IAV that is more consistent with our posterior flux estimate. Specifically, most GCP models fall within a narrow range of IAV, with 9 of the 11 prognostic GCP models and 13 of 16 diagnostic models having an IAV within the range of 10 % to 30 %. Although we do not have enough information to explain why the IAV of a few models fall outside this range (< 10 % or > 30 %), the overall pattern suggests that GCP models result in a lower and more consistent IAV compared to WETCHIMP models.

In contrast to our results, studies such as Thompson et al. (2017); Ward et al. (2024) find positive CH_4 flux trends, while studies like Sweeney et al. (2016a) find no significant long-term trends in CH_4 fluxes despite ongoing regional warming. These discrepancies in trends and IAV are likely driven by data sparsity and observational constraints. For example, differences in the spatial and temporal density of observation networks can skew trend detection, and sparse data coverage can yield spurious long-term trends on a sub-regional scale (Thompson et al., 2017; Ishizawa et al., 2024). Specifically, Ishizawa et al. (2024) found that when using limited observational data during an early study period, the model produced an upward trend in the Northern region and a downward trend in the Western region of Canada. However, when data coverage improved in later years, the overall trend across the two combined regions was no longer statistically significant. Similarly, some studies like Thompson et al. (2017) argue that earlier multi-year inverse models can fail to detect true trends, specifically because they lack a sufficient number of high-latitude observation sites to capture the signal.

https://doi.org/10.5194/egusphere-2026-6528
Preprint. Discussion started: 9 November 2026
© Author(s) 2026. CC BY 4.0 License.

Beyond inverse modeling studies, process-based models also disagree on IAV, and we hypothesize that IAV in inundation fraction is an important factor driving differences on IAV in CH_4 fluxes estimated by the GCP models. Eight of the eleven prognostic GCP models (CLASSIC, ELM, ISAM, JSBACH, JULES, LPJ-wsl, SDGVM, and VISIT) exhibit higher IAV than their corresponding diagnostic versions, and we focus on the prognostic GCP models in this analysis. To explore the relationship between inundation fraction and CH_4 fluxes, we create a scatter plot with the IAV of inundation fraction on the x-axis and the IAV of CH_4 fluxes on the y-axis for each available prognostic GCP model (Fig. S10). The prognostic GCP models suggest a modest positive relationship between the IAV of inundation fraction and that of CH_4 fluxes, although the relationship is not consistent across all models. In addition, we also compute the IAV for the inundation fraction maps simulated by the prognostic GCP models (Fig. S8). Among all models, JSBACH shows an exceptionally large flux IAV of 73 %, exceeding other models, including WETCHIMP (Fig. 5). Similarly, the inundation fraction map simulated by JSBACH also has the highest IAV (21.7 %) among the available prognostic inundation fraction maps (Fig. S8). In addition, the lower IAV estimated by diagnostic GCP models can be partly attributed to their use of the same inundation product (WAD2M v2). For example, the IAV of the WAD2M v2 inundation fraction map is 5.2 %, which is the second lowest IAV compared to all other inundation fraction maps estimated by prognostic GCP models. This low IAV in the WAD2M v2 inundation fraction map likely contributes to the similarly low IAV in CH_4 fluxes estimated by the diagnostic GCP models (Fig. 5). IAV in the diagnostic GCP models is similar to IAV in the flux estimate from the inverse model, and this result indicates that the WAD2M v2 product can possibly be used as a reliable inundation fraction map that constrains IAV in future process-based CH_4 flux model simulations.

3.3 Alaskan CH_4 fluxes peak in late summer during the May–September growing season

We find that the posterior CH_4 estimate and the mean of the WETCHIMP model ensemble peak in August, while flux estimates from the mean of the GCP model ensembles indicate a peak in July. A caveat to this result is that the difference between July and August estimates is not statistically significant. We calculate the mean monthly percentages of the total growing season fluxes (May to September) for our posterior estimate and for each process-based model ensemble over the years 2012–2015 and 2017 for GCP and 1993 to 2004 for WETCHIMP. Based on the shaded regions in Fig. 6, the GCP models have a much smaller inter-model spread compared to the WETCHIMP models. Specifically, the standard deviations of the mean monthly percentages for the GCP models range from 1.1 % to 3.4 %, compared with 4.7 % to 11.6 % for the WETCHIMP models and 3.0 % to 10.4 % for the posterior flux estimate. However, the similar monthly percentages shown by the GCP models do not necessarily indicate that they have improved skills in capturing the correct seasonal cycle. In fact, these GCP models allocate a larger fraction of total statewide CH_4 fluxes to early summer in June and July, which is different from the August peak in our posterior estimate.

3.4 Hydrological and carbon-related environmental drivers best explain CH_4 flux variability

We find that the environmental drivers that best explain the spatial and temporal variability of CH_4 fluxes within the Alaska domain are near-surface soil temperature and root-zone soil wetness. This combination of environmental driver variables yields the lowest BIC score: near-surface soil temperature at approximately 0.2 m depth (variable name TSOIL2) and root-zone

https://doi.org/10.5194/egusphere-2026-6528
Preprint. Discussion started: 9 November 2026
© Author(s) 2026. CC BY 4.0 License.

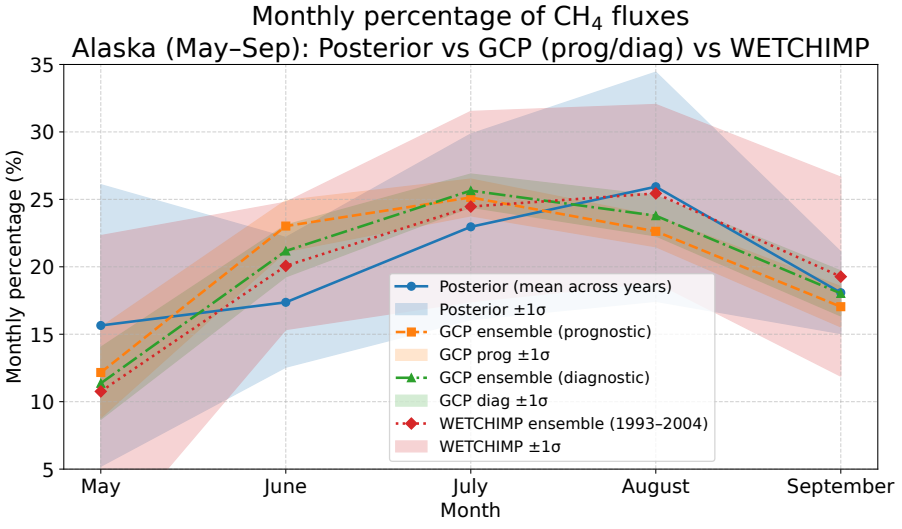


Figure 6. The mean monthly percentages of total May-September Alaska CH_4 fluxes for 2012 to 2015, and 2017 from the posterior estimate and process-based model ensembles. For each year, the monthly percentage is calculated as the total Alaska CH_4 flux in a given month divided by the total Alaska CH_4 flux summed over May-September and multiplied by 100. The shaded regions denote ± 1 standard deviation based on yearly variations for each type of the flux estimates.

soil wetness integrated over 0.1–1.0 m depth (variable name GWETROOT) (from Global Modeling and Assimilation Office (GMAO) (2015)). During model selection, we multiplied or interacted these variables with one another. Higher values of near-surface soil temperature provide favorable conditions for soil thaw and enhanced microbial activity, potentially increasing CH_4 fluxes when soils are wet and anaerobic. Root-zone soil wetness represents the amount of water content present in the soil layer where plant roots grow. Higher root-zone soil wetness values indicate wetter soils, which can restrict oxygen availability and create anaerobic conditions favorable for CH_4 production. Both of these variables are model-derived outputs from the Catchment Land Surface Model within the MERRA-2 reanalysis (Global Modeling and Assimilation Office (GMAO), 2015). Note that both of these variables are themselves model estimates with numerous uncertainties. Hence, although this combination of variables yields the lowest BIC score, it is neither a complete nor perfect model of CH_4 fluxes. Rather, we view it as a useful tool for understanding important environmental relationships.

This analysis illustrates that a simple combination of environmental drivers can be effective in describing spatial and temporal variability in CH_4 fluxes across broad regional scales in Alaska. Using our inverse model with the selected environmental drivers, we run the deterministic component through STILT and compare the modeled mixing ratios with atmospheric observations (Figs. 7 and S2). Based on Fig. 7, the estimated posterior fluxes in blue bars show a correlation coefficient of 0.92 and a RMSE of 11.8 ppb. The brown bars corresponding to the deterministic model indicate a correlation coefficient of 0.53 and an RMSE of 26.4 ppb. Note that this component represents the CH_4 fluxes predicted using near-surface soil temperature and root-zone soil wetness. The remaining portion of the flux variability is captured by the stochastic component, which accounts

https://doi.org/10.5194/egusphere-2026-6528
Preprint. Discussion started: 9 November 2026
© Author(s) 2026. CC BY 4.0 License.

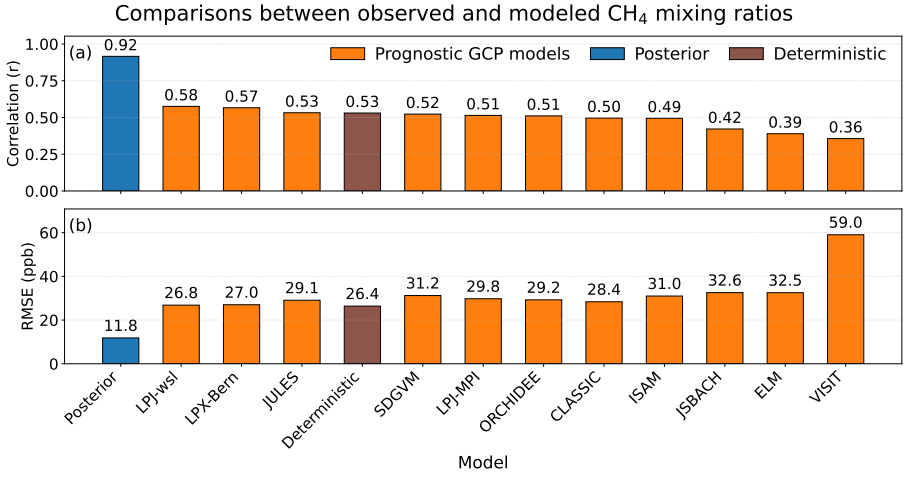


Figure 7. Model performance metrics when different flux estimates are run through WRF-STILT and compared with atmospheric CH_4 mixing ratios from the CARVE and Arctic-CAP aircraft campaigns. Higher correlation coefficients (panel a) and lower RMSE (panel b) indicate better agreement between observations and modeled mixing ratios.

for missing information that is not captured by environmental drivers. In contrast, the correlation coefficient values for all GCP models with prognostic runs are less than 0.58 and the RMSE values are all above 26.8 ppb. Among these GCP models, LPJ-wsl shows the best agreement with atmospheric observations, with a correlation coefficient of 0.58 and a RMSE of 26.8 ppb, consistent with a previous study that compares process-based models with atmospheric observations in Canada (Liu et al., 2026). Based on the comparisons, our deterministic component has correlation coefficient and RMSE values that are comparable to the best performing GCP models, suggesting that a simple combination of environmental drivers is effective in parameterizing large spatial and temporal patterns in CH_4 fluxes across Alaska. In addition, the deterministic component also reproduces the posterior hotspots over the Yukon–Kuskokwim Delta and the broader North Slope (Fig. 3b).

Several hypotheses may explain why a simple flux model is relatively effective at reproducing atmospheric CH_4 mixing ratios at the regional scale. First, the GCP process-based models are developed on a global scale, and the discrepancies revealed in this regional comparison suggest room for improvement in how these models represent high-latitude wetland CH_4 processes, particularly in Alaska. Second, the spatial distribution of CH_4 fluxes at regional scales may strongly depend on a few key environmental drivers, such as inundation fraction map, soil moisture, and soil carbon. If these large-scale driver data are inaccurate or poorly constrained, then global process-based models may struggle to reproduce the observed regional-scale CH_4 flux patterns. This finding implies that accurately representing a few salient environmental drivers may be one of the most important requirements for simulating regional-scale CH_4 flux patterns. By contrast, other aspects of the models, such as the completeness of process representation, may play a more important role in the performance of these models at finer spatial scales.

https://doi.org/10.5194/egusphere-2026-6528
Preprint. Discussion started: 9 November 2026
© Author(s) 2026. CC BY 4.0 License.

4 Conclusions

We estimate Alaskan CH_4 fluxes during the growing seasons (May–September) from 2012 to 2015 and in 2017 using atmospheric observations collected by the CARVE and Arctic-CAP aircraft campaigns. Our posterior flux estimate provides an observationally constrained benchmark that we use to evaluate the magnitudes, spatial distributions, seasonal cycles, and IAV of current and earlier global process-based wetland CH_4 flux models. This analysis shows that a simple flux model based on near-surface soil temperature and root-zone soil wetness can reproduce atmospheric observations comparably to more complex process-based models, suggesting that accurately representing a few salient environmental drivers may be one of the most important requirements for capturing regional-spatial patterns in CH_4 fluxes. The GCP models show better inter-model agreement on flux magnitudes and seasonality compared to earlier WETCHIMP models, indicating a narrower spread among model estimates. However, this greater agreement does not necessarily mean improved agreement with atmospheric observations, and our posterior flux estimate is 1.3 to 2.9 times higher than different ensembles of process-based models. In contrast, state-of-the-art GCP models show improvement in their spatial and IAV representations of Alaskan CH_4 fluxes compared to earlier WETCHIMP models. Specifically, GCP models show a larger contribution of the North Slope to total Alaskan CH_4 fluxes, which is more consistent with our estimates than WETCHIMP models. In addition, diagnostic GCP model ensemble exhibits an IAV similar to that of our estimates, reflecting that the WAD2M v2 inundation fraction map appears to provide a reliable benchmark for constraining IAV in process-based models. However, there are still opportunities for improvement in inundation fraction maps when it comes to future CH_4 flux model developments. While GCP models demonstrate improved inter-model agreement on flux magnitude and seasonality, earlier WETCHIMP models produce a magnitude and seasonality that is more consistent with our CH_4 flux estimate. As a result, our analysis shows that a key priority for reducing discrepancies between model-based and observation-based CH_4 flux estimates in Alaska is to improve the representation of soil wetness. Existing evidence suggests that current inundation maps may not skillfully represent soil wetness in some regions of Alaska. This need is especially important on the North Slope, where current inundation fraction maps may underestimate saturated areas that lack visible open water.

https://doi.org/10.5194/egusphere-2026-6528
Preprint. Discussion started: 9 November 2026
© Author(s) 2026. CC BY 4.0 License.

Data availability. We received the wetland model estimates from Zhen Zhang and the GCP modeling team, and these datasets are available upon request from the GCP modeling team. The CARVE dataset (2012–2015) is available through the NASA Earthdata catalog. The Arctic-CAP dataset (2017) is available through NASA Earthdata Search. The CARVE: L4 Gridded Footprints from the WRF-STILT model are available through NASA Earthdata Search. The ABoVE: Level-4 WRF-STILT Footprint Files for Circumpolar Receptors, 2016–2019 are available through NASA Earthdata Search. The EDGAR v6.0 Greenhouse Gas Emissions dataset is available through the European Commission Joint Research Centre data catalog. The Global Fire Emissions Database, Version 5.1 (GFEDv5), is available through Zenodo at GFEDv5. The gridded maps of geological CH_4 emissions dataset is available from Etiope et al. (2019). The Global-Gridded Daily Methane Emissions Climatology from Lake Systems, 2003–2015 dataset is available through NASA Earthdata Search. The Permafrost extent for the Northern Hemisphere, v4.0 from MODIS LST, ERA5, 1997-2021 is available through CEDA Archive.

Code and data availability. We used the GIM code from https://github.com/greenhousegaslab/geostatistical_inverse_modeling

Author contributions. HL and SMM designed the study and wrote the manuscript. CEM, CS, JDW, RC, LDS, ZZ, BP, LF, AC, WSD, VY, DH, and JRM provided feedback and comments on the manuscript. LF, AC, ZH, and DCG provided modeling support. JRM provided the WETCHIMP models. ZZ, BP, and the GCP modeling team provided the prognostic and diagnostic process-based CH_4 flux models.

Competing interests. The authors declare that they have no conflict of interest.

Acknowledgements. This work is funded by NASA ABoVE grant (#80NSSC22K1246) and by an NSF CAREER award (#2237404). A portion of this research was performed at the Jet Propulsion Laboratory, California Institute of Technology, under contract with National Aeronautics and Space Administration (#80NM0018D0004). We thank Oak Ridge National Laboratory DAAC (ORNL DAAC) and the ABoVE program for providing the CARVE and Arctic-CAP aircraft CH_4 dataset that is important for the completion of this work. The CARVE and Arctic-CAP data were acquired by the Carbon in Arctic Reservoirs Vulnerability Experiment (CARVE), an Earth Ventures Suborbital (EV-S1) investigation, under contract with the National Aeronautics and Space Administration. We also acknowledge the use of WRF-STILT footprints data that are produced as a part of the CarbonTracker-Lagrange project with the support from NOAA's Climate Program Office and NASA's Carbon Monitoring System. We use anthropogenic CH_4 fluxes from the EDGAR v6.0 Greenhouse Gas Emissions. We acknowledge the use of the fire fluxes from the Global Fire Emissions Database, Version 5.1 (GFEDv5) described in Randerson et al. (2017), and we regrid that dataset for this work. We also thank the Global Carbon Project (GCP) modeling team for their invaluable contributions in developing the models. In addition, we specifically thank the following individuals for their important work in building the GCP models: Benjamin Poulter, Philippe Ciais, Joe Melton, William Riley, David Beerling, Nicola Gedney, Peter Hopcroft, Akihiko Ito, Atul Jain, Fortunat Joos, Thomas Kleinen, Tingting Li, Xiangyu Liu, Paul Miller, Changhui Peng, Shushi Peng, Zhangcai Qin, Qing Sun, Hanqin Tian, Yi Xi, Wenxin Zhang, Qing Zhu, Qiuan Zhu, and Qianlai Zhuang.

https://doi.org/10.5194/egusphere-2026-6528
Preprint. Discussion started: 9 November 2026
© Author(s) 2026. CC BY 4.0 License.

References

Bayesian Information Criteria, pp. 211–237, Springer New York, New York, NY, ISBN 978-0-387-71887-3, https://doi.org/10.1007/978-0-387-71887-3_9, 2008.

Bergamaschi, P., Frankenberg, C., Meirink, J. F., Krol, M., Dentener, F., Wagner, T., Platt, U., Kaplan, J. O., Körner, S., Heimann, M., Dlugokencky, E. J., and Goede, A.: Satellite chartography of atmospheric methane from SCIAMACHY on board ENVISAT: 2. Evaluation based on inverse model simulations, J. Geophys. Res.-Atmos., 112, https://doi.org/10.1029/2006JD007268, 2007.

Bernard, J., Prigent, C., Jimenez, C., Fluet-Chouinard, E., Lehner, B., Salmon, E., Ciais, P., Zhang, Z., Peng, S., and Saunois, M.: The GIEMS-MethaneCentric database: a dynamic and comprehensive global product of methane-emitting aquatic areas, Earth Syst. Sci. Data, 17, 2985–3008, https://doi.org/10.5194/essd-17-2985-2025, 2025a.

Bernard, J., Salmon, E., Saunois, M., Peng, S., Serrano-Ortiz, P., Berchet, A., Gnanamoorthy, P., Jansen, J., and Ciais, P.: Satellite-based modeling of wetland methane emissions on a global scale (SatWetCH4 1.0), Geosci. Model Dev., 18, 863–883, https://doi.org/10.5194/gmd-18-863-2025, 2025b.

Bohn, T. J., Melton, J. R., Ito, A., Kleinen, T., Spahni, R., Stocker, B. D., Zhang, B., Zhu, X., Schroeder, R., Glagolev, M. V., Maksyutov, S., Brovkin, V., Chen, G., Denisov, S. N., Eliseev, A. V., Gallego-Sala, A., McDonald, K. C., Rawlins, M. A., Riley, W. J., Subin, Z. M., Tian, H., Zhuang, Q., and Kaplan, J. O.: WETCHIMP-WSL: intercomparison of wetland methane emissions models over West Siberia, Biogeosciences, 12, 3321–3349, https://doi.org/10.5194/bg-12-3321-2015, 2015.

Chang, R. Y.-W., Miller, C. E., Dinardo, S. J., Karion, A., Sweeney, C., Daube, B. C., Henderson, J. M., Mountain, M. E., Eluszkiewicz, J., Miller, J. B., Bruhwiler, L. M. P., and Wofsy, S. C.: Methane emissions from Alaska in 2012 from CARVE airborne observations, P. Natl. Acad. Sci. USA, 111, 16 694–16 699, https://doi.org/10.1073/pnas.1412953111, 2014a.

Chang, R. Y.-W., Miller, C. E., Dinardo, S. J., Karion, A., Sweeney, C., Daube, B. C., Henderson, J. M., Mountain, M. E., Eluszkiewicz, J., Miller, J. B., Bruhwiler, L. M. P., and Wofsy, S. C.: Methane emissions from Alaska in 2012 from CARVE airborne observations, P. Natl. Acad. Sci. USA, 111, 16 694–16 699, https://doi.org/10.1073/pnas.1412953111, 2014b.

Chen, A., Zhang, Z., Poulter, B., Feng, L., Liu, H., Murray, L. T., Yu, X., Huang, Z., Gaeta, D. C., Morgan, K. L., Zhu, Q., and Miller, S. M.: Spatial and temporal distribution of global wetland methane emissions during 2019–2020 estimated from satellite observations, J. Geophys. Res.-Atmos., 130, e2025JD044 354, https://doi.org/10.1029/2025JD044354, e2025JD044354 2025JD044354, 2025.

Commane, R., Lindaas, J., Benmergui, J., Luus, K. A., Chang, R. Y.-W., Daube, B. C., Euskirchen, E. S., Henderson, J. M., Karion, A., Miller, J. B., Miller, S. M., Parazoo, N. C., Randerson, J. T., Sweeney, C., Tans, P., Thoning, K., Veraverbeke, S., Miller, C. E., and Wofsy, S. C.: Carbon dioxide sources from Alaska driven by increasing early winter respiration from Arctic tundra, P. Natl. Acad. Sci. USA, 114, 5361–5366, https://doi.org/10.1073/pnas.1618567114, 2017.

Council, N. R.: Opportunities to use remote sensing in understanding permafrost and related ecological characteristics: report of a workshop, The National Academies Press, Washington, DC, ISBN 978-0-309-30121-3, https://doi.org/10.17226/18711, 2014.

Crippa, M., Guizzardi, D., Muntean, M., Schaaf, E., Lo Vullo, E., Solazzo, E., Monforti-Ferrario, F., Olivier, J., and Vignati, E.: EDGAR v6.0 Greenhouse Gas Emissions, https://doi.org/10.2905/JRC.787T5VR, dataset, 2026.

Cucchi, M., Weedon, G. P., Amici, A., Bellouin, N., Lange, S., Müller Schmied, H., Hersbach, H., and Buontempo, C.: WFDE5: bias-adjusted ERA5 reanalysis data for impact studies, Earth Syst. Sci. Data, 12, 2097–2120, https://doi.org/10.5194/essd-12-2097-2020, 2020.

Dirmeyer, P. A., Gao, X., Zhao, M., Guo, Z., Oki, T., and Hanasaki, N.: GSWP-2: multimodel analysis and implications for our perception of the land surface, B. Am. Meteorol. Soc., 87, 1381–1398, https://doi.org/10.1175/BAMS-87-10-1381, 2006.

https://doi.org/10.5194/egusphere-2026-6528
Preprint. Discussion started: 9 November 2026
© Author(s) 2026. CC BY 4.0 License.

Dong, B., Peng, S., Liu, G., Pu, T., Gerlein-Safdi, C., Prigent, C., and Lin, X.: Underestimation of methane emissions from the Sudd wetland: unraveling the impact of wetland extent dynamics, Geophys. Res. Lett., 51, e2024GL110 690, https://doi.org/10.1029/2024GL110690, e2024GL110690 2024GL110690, 2024.

Etiope, G., Ciotoli, G., Schwietzke, S., and Schoell, M.: Gridded maps of geological methane emissions and their isotopic signature, Earth Syst. Sci. Data, 11, 1–22, https://doi.org/10.5194/essd-11-1-2019, 2019.

Fang, Y. and Michalak, A. M.: Atmospheric observations inform CO_2 flux responses to enviroclimatic drivers, Global Biogeochem. Cy., 29, 555–566, https://doi.org/10.1002/2014GB005034, 2015.

Feng, L., Tavakkoli, S., Jordaan, S. M., Andrews, A. E., Benmergui, J. S., Waugh, D. W., Zhang, M., Gaeta, D. C., and Miller, S. M.: Inter-annual variability in atmospheric transport complicates estimation of US methane emissions trends, Geophys. Res. Lett., 50, e2022GL100 366, https://doi.org/10.1029/2022GL100366, e2022GL100366 2022GL100366, 2023.

Fisher, J. B., Sikka, M., Oechel, W. C., Huntzinger, D. N., Melton, J. R., Koven, C. D., Ahlström, A., Arain, M. A., Baker, I., Chen, J. M., Ciais, P., Davidson, C., Dietze, M., El-Masri, B., Hayes, D., Huntingford, C., Jain, A. K., Levy, P. E., Lomas, M. R., Poulter, B., Price, D., Sahoo, A. K., Schaefer, K., Tian, H., Tomelleri, E., Verbeeck, H., Viovy, N., Wania, R., Zeng, N., and Miller, C. E.: Carbon cycle uncertainty in the Alaskan Arctic, Biogeosciences, 11, 4271–4288, https://doi.org/10.5194/bg-11-4271-2014, 2014.

Friedlingstein, P., O'Sullivan, M., Jones, M. W., Andrew, R. M., Hauck, J., Landschützer, P., Le Quéré, C., Li, H., Luijkx, I. T., Olsen, A., Peters, G. P., Peters, W., Pongratz, J., Schwingshackl, C., Sitch, S., Canadell, J. G., Ciais, P., Jackson, R. B., Alin, S. R., Arneth, A., Arora, V., Bates, N. R., Becker, M., Bellouin, N., Berghoff, C. F., Bittig, H. C., Bopp, L., Cadule, P., Campbell, K., Chamberlain, M. A., Chandra, N., Chevallier, F., Chini, L. P., Colligan, T., Decayeux, J., Djeutchouang, L. M., Dou, X., Duran Rojas, C., Enyo, K., Evans, W., Fay, A. R., Feely, R. A., Ford, D. J., Foster, A., Gasser, T., Gehlen, M., Gkritzalis, T., Grassi, G., Gregor, L., Gruber, N., Gürses, O., Harris, I., Hefner, M., Heinke, J., Hurtt, G. C., Iida, Y., Ilyina, T., Jacobson, A. R., Jain, A. K., Jarníková, T., Jersild, A., Jiang, F., Jin, Z., Kato, E., Keeling, R. F., Klein Goldewijk, K., Knauer, J., Korsbakken, J. I., Lan, X., Lauvset, S. K., Lefèvre, N., Liu, Z., Liu, J., Ma, L., Maksyutov, S., Marland, G., Mayot, N., McGuire, P. C., Metzl, N., Monacci, N. M., Morgan, E. J., Nakaoka, S.-I., Neill, C., Niwa, Y., Nützel, T., Olivier, L., Ono, T., Palmer, P. I., Pierrot, D., Qin, Z., Resplandy, L., Roobaert, A., Rosan, T. M., Rödenbeck, C., Schwinger, J., Smallman, T. L., Smith, S. M., Sospedra-Alfonso, R., Steinhoff, T., Sun, Q., Sutton, A. J., Séférian, R., Takao, S., Tatebe, H., Tian, H., Tilbrook, B., Torres, O., Tourigny, E., Tsujino, H., Tubiello, F., van der Werf, G., Wanninkhof, R., Wang, X., Yang, D., Yang, X., Yu, Z., Yuan, W., Yue, X., Zaehle, S., Zeng, N., and Zeng, J.: Global Carbon Budget 2024, Earth Syst. Sci. Data, 17, 965–1039, https://doi.org/10.5194/essd-17-965-2025, 2025.

Fujita, R., Morimoto, S., Umezawa, T., Ishijima, K., Patra, P. K., Worthy, D. E. J., Goto, D., Aoki, S., and Nakazawa, T.: Temporal variations of the mole fraction, carbon, and hydrogen isotope ratios of atmospheric methane in the Hudson Bay Lowlands, Canada, J. Geophys. Res.-Atmos., 123, 4695–4711, https://doi.org/10.1002/2017JD027972, 2018.

Fung, I., John, J., Lerner, J., Matthews, E., Prather, M., Steele, L. P., and Fraser, P. J.: Three-dimensional model synthesis of the global methane cycle, J. Geophys. Res.-Atmos., 96, 13 033–13 065, https://doi.org/10.1029/91JD01247, 1991.

Gaeta, D. C., Mühle, J., Vimont, I. J., Crotwell, M., Hu, L., Miller, J. B., McKain, K., Baier, B. C., Zhang, M., Bao, J., Miller, B. R., and Miller, S. M.: California dominates U.S. emissions of the pesticide and potent greenhouse gas sulfuryl fluoride, Commun. Earth Environ., 5, 161, https://doi.org/10.1038/s43247-024-01294-x, 2024.

Gao, M., Xing, Z., Vollrath, C., Hugenholtz, C. H., and Barchyn, T. E.: Global observational coverage of on-shore oil and gas methane sources with TROPOMI, Sci. Rep.-UK, 13, 16 759, https://doi.org/10.1038/s41598-023-41914-8, 2023.

https://doi.org/10.5194/egusphere-2026-6528
Preprint. Discussion started: 9 November 2026
© Author(s) 2026. CC BY 4.0 License.

Gelaro, R., McCarty, W., Suárez, M. J., Todling, R., Molod, A., Takacs, L., Randles, C. A., Darmenov, A., Bosilovich, M. G., Reichle, R., Wargan, K., Coy, L., Cullather, R., Draper, C., Akella, S., Buchard, V., Conaty, A., da Silva, A. M., Gu, W., Kim, G.-K., Koster, R., Lucchesi, R., Merkova, D., Nielsen, J. E., Partyka, G., Pawson, S., Putman, W., Rienecker, M., Schubert, S. D., Sienkiewicz, M., and Zhao, B.: The Modern-Era Retrospective Analysis for Research and Applications, Version 2 (MERRA-2), J. Climate, 30, 5419–5454, https://doi.org/10.1175/JCLI-D-16-0758.1, 2017.

Global Modeling and Assimilation Office (GMAO): MERRA-2 tavg1_2d_lnd_Nx: 2d, 1-Hourly, Time-Averaged, Single-Level, Assimilation, Land Surface Diagnostics V5.12.4, https://doi.org/10.5067/RKPHT8KC1Y1T, 2015.

Gourdji, S. M., Mueller, K. L., Yadav, V., Huntzinger, D. N., Andrews, A. E., Trudeau, M., Petron, G., Nehrkorn, T., Eluszkiewicz, J., Henderson, J., Wen, D., Lin, J., Fischer, M., Sweeney, C., and Michalak, A. M.: North American CO_2 exchange: inter-comparison of modeled estimates with results from a fine-scale atmospheric inversion, Biogeosciences, 9, 457–475, https://doi.org/10.5194/bg-9-457-2012, 2012.

Grasset, C., Mesman, J. P., Tranvik, L. J., Maranger, R., and Sobek, S.: Contribution of lake littoral zones to the continental carbon budget, Nat. Geosci., 18, 747–752, https://doi.org/10.1038/s41561-025-01739-8, 2025.

Guo, H.-X., Zhu, W.-Q., Xiao, C.-D., Zhao, C.-L., and Chen, L.-Y.: The freezing–thawing index and permafrost extent in pan-Arctic experienced rapid changes following the global warming hiatus, Adv. Clim. Change Res., 16, 350–360, https://doi.org/10.1016/j.accre.2025.02.010, special topic on changing periglacial and aeolian landscapes, 2025.

Harris, I., Jones, P., and Osborn, T.: CRU TS4.06: Climatic Research Unit (CRU) Time-Series (TS) version 4.06 of high-resolution gridded data of month-by-month variation in climate (Jan. 1901 - Dec. 2021), NERC EDS Centre for Environmental Data Analysis, https://catalogue.ceda.ac.uk/uuid/e0b4e1e56c1c4460b796073a31366980/, 2022.

Hartery, S., Commane, R., Lindaas, J., Sweeney, C., Henderson, J., Mountain, M., Steiner, N., McDonald, K., Dinardo, S. J., Miller, C. E., Wofsy, S. C., and Chang, R. Y.-W.: Estimating regional-scale methane flux and budgets using CARVE aircraft measurements over Alaska, Atmos. Chem. Phys., 18, 185–202, https://doi.org/10.5194/acp-18-185-2018, 2018.

Henderson, J., Miller, J. B., Nehrkorn, T., Chang, R. Y.-W., Sweeney, C., Steiner, N., Wofsy, S. C., and Miller, C. E.: CARVE: L4 Gridded Footprints from WRF-STILT model, 2012-2016, https://doi.org/10.3334/ORNLDAAC/1431, date Accessed: 2025-11-21, 2017.

Henderson, J., Mountain, M., Dayalu, A., McKain, K., Hu, L., and Nehrkorn, T.: ABoVE: Level-4 WRF-STILT Footprint Files for Circumpolar Receptors, 2016-2019, https://doi.org/10.3334/ORNLDAAC/1896, date Accessed: 2025-11-21, 2021.

Henderson, J. M., Eluszkiewicz, J., Mountain, M. E., Nehrkorn, T., Chang, R. Y.-W., Karion, A., Miller, J. B., Sweeney, C., Steiner, N., Wofsy, S. C., and Miller, C. E.: Atmospheric transport simulations in support of the Carbon in Arctic Reservoirs Vulnerability Experiment (CARVE), Atmos. Chem. Phys., 15, 4093–4116, https://doi.org/10.5194/acp-15-4093-2015, 2015.

Hodson, E. L., Poulter, B., Zimmermann, N. E., Prigent, C., and Kaplan, J. O.: The El Niño–Southern Oscillation and wetland methane interannual variability, Geophys. Res. Lett., 38, https://doi.org/10.1029/2011GL046861, 2011.

Hugelius, G., Strauss, J., Zubrzycki, S., Harden, J. W., Schuur, E. A. G., Ping, C.-L., Schirrmeister, L., Grosse, G., Michaelson, G. J., Koven, C. D., O'Donnell, J. A., Elberling, B., Mishra, U., Camill, P., Yu, Z., Palmtag, J., and Kuhry, P.: Estimated stocks of circumpolar permafrost carbon with quantified uncertainty ranges and identified data gaps, Biogeosciences, 11, 6573–6593, https://doi.org/10.5194/bg-11-6573-2014, 2014.

Ishizawa, M., Chan, D., Worthy, D., Chan, E., Vogel, F., Melton, J. R., and Arora, V. K.: Estimation of Canada's methane emissions: inverse modelling analysis using the Environment and Climate Change Canada (ECCC) measurement network, Atmos. Chem. Phys., 24, 10 013–10 038, https://doi.org/10.5194/acp-24-10013-2024, 2024.

https://doi.org/10.5194/egusphere-2026-6528
Preprint. Discussion started: 9 November 2026
© Author(s) 2026. CC BY 4.0 License.

Ito, A. and Inatomi, M.: Use of a process-based model for assessing the methane budgets of global terrestrial ecosystems and evaluation of uncertainty, Biogeosciences, 9, 759–773, https://doi.org/10.5194/bg-9-759-2012, 2012.

Ito, A., Li, T., Qin, Z., Melton, J. R., Tian, H., Kleinen, T., Zhang, W., Zhang, Z., Joos, F., Ciais, P., Hopcroft, P. O., Beerling, D. J., Liu, X., Zhuang, Q., Zhu, Q., Peng, C., Chang, K.-Y., Fluet-Chouinard, E., McNicol, G., Patra, P., Poulter, B., Sitch, S., Riley, W., and Zhu, Q.: Cold-season methane fluxes simulated by GCP-CH_4 models, Geophys. Res. Lett., 50, e2023GL103 037, https://doi.org/10.1029/2023GL103037, e2023GL103037 2023GL103037, 2023.

Jeong, S., Zhao, C., Andrews, A. E., Bianco, L., Wilczak, J. M., and Fischer, M. L.: Seasonal variation of CH_4 emissions from central California, J. Geophys. Res.-Atmos., 117, https://doi.org/10.1029/2011JD016896, 2012.

Johnson, M. S., Matthews, E., Bastviken, D., Du, J., and Genovese, V.: Global-gridded daily methane emissions climatology from lake systems, 2003–2015, https://doi.org/10.3334/ORNLDAAC/2008, last access: 22 May 2026, 2022.

Jorgenson, M. T., Yoshikawa, K., Kanevskiy, M. Z., Shur, Y. L., Romanovsky, V. E., Marchenko, S. S., Grosse, G., Brown, J., and Jones, B. M.: Permafrost characteristics of Alaska, in: Proceedings of the Ninth International Conference on Permafrost, edited by Kane, D. L. and Hinkel, K. M., pp. 121–122, Institute of Northern Engineering, University of Alaska Fairbanks, https://dggs.alaska.gov/pubs/id/29801, 2008.

Kim, H.: Global Soil Wetness Project Phase 3 Atmospheric Boundary Conditions (Experiment 1), https://doi.org/10.20783/DIAS.501, 2017.

Kleinen, T., Mikolajewicz, U., and Brovkin, V.: Terrestrial methane emissions from the Last Glacial Maximum to the preindustrial period, Clim. Past, 16, 575–595, https://doi.org/10.5194/cp-16-575-2020, 2020.

Kyzivat, E. D. and Smith, L. C.: A closer look at the effects of lake area, aquatic vegetation, and double-counted wetlands on Pan-Arctic lake methane emissions estimates, Geophys. Res. Lett., 50, e2023GL104 825, https://doi.org/10.1029/2023GL104825, e2023GL104825 2023GL104825, 2023.

Lane, C. R., D'Amico, E., Christensen, J. R., Golden, H. E., Wu, Q., and Rajib, A.: Mapping global non-floodplain wetlands, Earth Syst. Sci. Data, 15, 2927–2955, https://doi.org/10.5194/essd-15-2927-2023, 2023.

Lange, S., Menz, C., Gleixner, S., Cucchi, M., Weedon, G. P., Amici, A., Bellouin, N., Müller-Schmied, H., Hersbach, H., Buontempo, C., and Cagnazzo, C.: WFDE5 over land merged with ERA5 over the ocean (W5E5 v2.0), ISIMIP Repository, https://doi.org/10.48364/ISIMIP.342217, 2021.

Li, Z.-C., Sun, W.-B., Liang, C.-X., Xing, X.-H., and Li, Q.-X.: Arctic warming trends and their uncertainties based on surface temperature reconstruction under different sea ice extent scenarios, Adv. Clim. Change Res., 14, 335–346, https://doi.org/10.1016/j.accre.2023.06.003, 2023.

Lin, J. C., Gerbig, C., Wofsy, S. C., Andrews, A. E., Daube, B. C., Davis, K. J., and Grainger, C. A.: A near-field tool for simulating the upstream influence of atmospheric observations: The Stochastic Time-Inverted Lagrangian Transport (STILT) model, J. Geophys. Res.-Atmos., 108, https://doi.org/10.1029/2002JD003161, 2003.

Liu, H., Ishizawa, M., Vogel, F. R., Zhang, Z., Poulter, B., Feng, L., Chen, A., Gagné-Landmann, A. L., Huntzinger, D. N., Melton, J. R., Yadav, V., Gaeta, D. C., Huang, Z., Worthy, D. E. J., Chan, D., and Miller, S. M.: Methane fluxes from Arctic & boreal North America: comparisons between process-based estimates and atmospheric observations, Atmospheric Chemistry and Physics, 26, 1229–1247, https://doi.org/10.5194/acp-26-1229-2026, 2026.

Liu, X. and Zhuang, Q.: Methane emissions from Arctic landscapes during 2000–2015: an analysis with land and lake biogeochemistry models, Biogeosciences, 20, 1181–1193, https://doi.org/10.5194/bg-20-1181-2023, 2023a.

https://doi.org/10.5194/egusphere-2026-6528
Preprint. Discussion started: 9 November 2026
© Author(s) 2026. CC BY 4.0 License.



Liu, X. and Zhuang, Q.: Methane emissions from Arctic landscapes during 2000–2015: an analysis with land and lake biogeochemistry models, Biogeosciences, 20, 1181–1193, https://doi.org/10.5194/bg-20-1181-2023, 2023b.

MacGilchrist, G., Naveira Garabato, A., Tsubouchi, T., Bacon, S., Torres-Valdés, S., and Azetsu-Scott, K.: The Arctic Ocean carbon sink, Deep-Sea Res. Pt. I, 86, 39–55, https://doi.org/10.1016/j.dsr.2014.01.002, 2014.

Marthews, T. R., Dadson, S. J., Clark, D. B., Blyth, E. M., Hayman, G. D., Yamazaki, D., Becher, O. R. E., Martínez-de la Torre, A., Prigent, C., and Jiménez, C.: Inundation prediction in tropical wetlands from JULES-CaMa-Flood global land surface simulations, Hydrol. Earth Syst. Sci., 26, 3151–3175, https://doi.org/10.5194/hess-26-3151-2022, 2022.

Matthews, E. and Fung, I.: Methane emission from natural wetlands: Global distribution, area, and environmental characteristics of sources, Global Biogeochem. Cy., 1, 61–86, https://doi.org/10.1029/GB001i001p00061, 1987.

McKain, K., Down, A., Raciti, S. M., Budney, J., Hutyra, L. R., Floerchinger, C., Herndon, S. C., Nehrkorn, T., Zahniser, M. S., Jackson, R. B., Phillips, N., and Wofsy, S. C.: Methane emissions from natural gas infrastructure and use in the urban region of Boston, Massachusetts, P. Natl. Acad. Sci. USA, 112, 1941–1946, https://doi.org/10.1073/pnas.1416261112, 2015.

Melack, J. M. and Hess, L. L.: Areal extent of vegetative cover: A challenge to regional upscaling of methane emissions, Aquat. Bot., 184, 103 592, https://doi.org/10.1016/j.aquabot.2022.103592, 2023.

Melton, J. R., Wania, R., Hodson, E. L., Poulter, B., Ringeval, B., Spahni, R., Bohn, T., Avis, C. A., Beerling, D. J., Chen, G., Eliseev, A. V., Denisov, S. N., Hopcroft, P. O., Lettenmaier, D. P., Riley, W. J., Singarayer, J. S., Subin, Z. M., Tian, H., Zürcher, S., Brovkin, V., van Bodegom, P. M., Kleinen, T., Yu, Z. C., and Kaplan, J. O.: Present state of global wetland extent and wetland methane modelling: conclusions from a model inter-comparison project (WETCHIMP), Biogeosciences, 10, 753–788, https://doi.org/10.5194/bg-10-753-2013, 2013.

Michalak, A. M., Bruhwiler, L., and Tans, P. P.: A geostatistical approach to surface flux estimation of atmospheric trace gases, J. Geophys. Res.-Atmos., 109, https://doi.org/10.1029/2003JD004422, 2004.

Miller, S. M., Wofsy, S. C., Michalak, A. M., Kort, E. A., Andrews, A. E., Biraud, S. C., Dlugokencky, E. J., Eluszkiewicz, J., Fischer, M. L., Janssens-Maenhout, G., Miller, B. R., Miller, J. B., Montzka, S. A., Nehrkorn, T., and Sweeney, C.: Anthropogenic emissions of methane in the United States, P. Natl. Acad. Sci. USA, 110, 20 018–20 022, https://doi.org/10.1073/pnas.1314392110, 2013.

Miller, S. M., Worthy, D. E. J., Michalak, A. M., Wofsy, S. C., Kort, E. A., Havice, T. C., Andrews, A. E., Dlugokencky, E. J., Kaplan, J. O., Levi, P. J., Tian, H., and Zhang, B.: Observational constraints on the distribution, seasonality, and environmental predictors of North American boreal methane emissions, Global Biogeochem. Cy., 28, 146–160, https://doi.org/10.1002/2013GB004580, 2014.

Miller, S. M., Commane, R., Melton, J. R., Andrews, A. E., Benmergui, J., Dlugokencky, E. J., Janssens-Maenhout, G., Michalak, A. M., Sweeney, C., and Worthy, D. E. J.: Evaluation of wetland methane emissions across North America using atmospheric data and inverse modeling, Biogeosciences, 13, 1329–1339, https://doi.org/10.5194/bg-13-1329-2016, 2016a.

Miller, S. M., Miller, C. E., Commane, R., Chang, R. Y.-W., Dinardo, S. J., Henderson, J. M., Karion, A., Lindaas, J., Melton, J. R., Miller, J. B., Sweeney, C., Wofsy, S. C., and Michalak, A. M.: A multiyear estimate of methane fluxes in Alaska from CARVE atmospheric observations, Global Biogeochem. Cy., 30, 1441–1453, https://doi.org/10.1002/2016GB005419, 2016b.

Miller, S. M., Miller, C. E., Commane, R., Chang, R. Y.-W., Dinardo, S. J., Henderson, J. M., Karion, A., Lindaas, J., Melton, J. R., Miller, J. B., Sweeney, C., Wofsy, S. C., and Michalak, A. M.: A multiyear estimate of methane fluxes in Alaska from CARVE atmospheric observations, Global Biogeochem. Cy., 30, 1441–1453, https://doi.org/10.1002/2016GB005419, 2016c.

Miller, S. M., Michalak, A. M., Yadav, V., and Tadić, J. M.: Characterizing biospheric carbon balance using CO_2 observations from the OCO-2 satellite, Atmos. Chem. Phys., 18, 6785–6799, https://doi.org/10.5194/acp-18-6785-2018, 2018.

https://doi.org/10.5194/egusphere-2026-6528
Preprint. Discussion started: 9 November 2026
© Author(s) 2026. CC BY 4.0 License.



Miller, S. M., Saibaba, A. K., Trudeau, M. E., Mountain, M. E., and Andrews, A. E.: Geostatistical inverse modeling with very large datasets: an example from the Orbiting Carbon Observatory 2 (OCO-2) satellite, Geosci. Model Dev., 13, 1771–1785, https://doi.org/10.5194/gmd-13-1771-2020, 2020.

Muster, S., Heim, B., Abnizova, A., and Boike, J.: Water body distributions across scales: a remote sensing based comparison of three Arctic tundra wetlands, Remote Sens., 5, 1498–1523, https://doi.org/10.3390/rs5041498, 2013.

Neath, A. A. and Cavanaugh, J. E.: The Bayesian information criterion: background, derivation, and applications, WIREs Comput. Stat., 4, 199–203, https://doi.org/10.1002/wics.199, 2012.

Peng, X., Zhang, T., Frauenfeld, O. W., Mu, C., Wang, K., Wu, X., Guo, D., Luo, J., Hjort, J., Aalto, J., Karjalainen, O., and Luoto, M.: Active layer thickness and permafrost area projections for the 21st century, Earth's Future, 11, e2023EF003 573, https://doi.org/10.1029/2023EF003573, e2023EF003573 2023EF003573, 2023.

Penny, W., Mattout, J., and Trujillo-Barreto, N.: CHAPTER 35 - Bayesian model selection and averaging, in: Statistical Parametric Mapping, edited by Friston, K., Ashburner, J., Kiebel, S., Nichols, T., and Penny, W., pp. 454–467, Academic Press, London, ISBN 978-0-12-372560-8, https://doi.org/10.1016/B978-012372560-8/50035-8, 2007.

Pickett-Heaps, C. A., Jacob, D. J., Wecht, K. J., Kort, E. A., Wofsy, S. C., Diskin, G. S., Worthy, D. E. J., Kaplan, J. O., Bey, I., and Drevet, J.: Magnitude and seasonality of wetland methane emissions from the Hudson Bay Lowlands (Canada), Atmos. Chem. Phys., 11, 3773–3779, https://doi.org/10.5194/acp-11-3773-2011, 2011.

Prigent, C., Papa, F., Aires, F., Rossow, W. B., and Matthews, E.: Global inundation dynamics inferred from multiple satellite observations, 1993–2000, J. Geophys. Res.-Atmos., 112, https://doi.org/10.1029/2006JD007847, 2007.

Randerson, J. T., van der Werf, G. R., Giglio, L., Collatz, G. J., and Kasibhatla, P. S.: Global Fire Emissions Database, Version 4.1 (GFEDv4.1), https://doi.org/10.3334/ORNLDAAC/1293, date accessed: 2025-11-21, 2017.

Rantanen, M., Karpechko, A. Y., Lipponen, A., Nordling, K., Hyvärinen, O., Ruosteenoja, K., Vihma, T., and Laaksonen, A.: The Arctic has warmed nearly four times faster than the globe since 1979, Commun. Earth Environ., 3, 168, https://doi.org/10.1038/s43247-022-00498-3, 2022.

Riley, W. J., Subin, Z. M., Lawrence, D. M., Swenson, S. C., Torn, M. S., Meng, L., Mahowald, N. M., and Hess, P.: Barriers to predicting changes in global terrestrial methane fluxes: analyses using CLM4Me, a methane biogeochemistry model integrated in CESM, Biogeosciences, 8, 1925–1953, https://doi.org/10.5194/bg-8-1925-2011, 2011.

Rosen, P. A., Bawden, G. W., Barela, P., Chapman, B., Fattahi, H., Jones, C. E., Joughin, I. R., Lavalle, M., Lohman, R. B., Simons, M., Siqueira, P., Das, A., Desai, N. M., Kumar, R., Putrevu, D., Sharma, R., and Shrikant, C.: The NASA-ISRO SAR Mission: A summary, IEEE Geosci. Remote Sens. Mag., 13, 8–34, https://doi.org/10.1109/MGRS.2025.3578258, 2025.

Rößger, N., Sachs, T., Wille, C., Boike, J., and Kutzbach, L.: Seasonal increase of methane emissions linked to warming in Siberian tundra, Nat. Clim. Change, 12, 1031–1036, https://doi.org/10.1038/s41558-022-01512-4, 2022.

Saunois, M., Martinez, A., Poulter, B., Zhang, Z., Raymond, P. A., Regnier, P., Canadell, J. G., Jackson, R. B., Patra, P. K., Bousquet, P., Ciais, P., Dlugokencky, E. J., Lan, X., Allen, G. H., Bastviken, D., Beerling, D. J., Belikov, D. A., Blake, D. R., Castaldi, S., Crippa, M., Deemer, B. R., Dennison, F., Etiope, G., Gedney, N., Höglund-Isaksson, L., Holgerson, M. A., Hopcroft, P. O., Hugelius, G., Ito, A., Jain, A. K., Janardanan, R., Johnson, M. S., Kleinen, T., Krummel, P. B., Lauerwald, R., Li, T., Liu, X., McDonald, K. C., Melton, J. R., Mühle, J., Müller, J., Murguia-Flores, F., Niwa, Y., Noce, S., Pan, S., Parker, R. J., Peng, C., Ramonet, M., Riley, W. J., Rocher-Ros, G., Rosentreter, J. A., Sasakawa, M., Segers, A., Smith, S. J., Stanley, E. H., Thanwerdas, J., Tian, H., Tsuruta, A., Tubiello, F. N., Weber,

https://doi.org/10.5194/egusphere-2026-6528
Preprint. Discussion started: 9 November 2026
© Author(s) 2026. CC BY 4.0 License.

T. S., van der Werf, G. R., Worthy, D. E. J., Xi, Y., Yoshida, Y., Zhang, W., Zheng, B., Zhu, Q., Zhu, Q., and Zhuang, Q.: Global Methane Budget 2000–2020, Earth Syst. Sci. Data, 17, 1873–1958, https://doi.org/10.5194/essd-17-1873-2025, 2025.

Schaefer, K., Zhang, T., Bruhwiler, L., and Barrett, A. P.: Amount and timing of permafrost carbon release in response to climate warming, Tellus B, 63, 165–180, https://doi.org/10.1111/j.1600-0889.2011.00527.x, 2011.

Schiferl, L. D., Watts, J. D., Larson, E. J. L., Arndt, K. A., Biraud, S. C., Euskirchen, E. S., Goodrich, J. P., Henderson, J. M., Kalhori, A., McKain, K., Mountain, M. E., Munger, J. W., Oechel, W. C., Sweeney, C., Yi, Y., Zona, D., and Commane, R.: Using atmospheric observations to quantify annual biogenic carbon dioxide fluxes on the Alaska North Slope, Biogeosciences, 19, 5953–5972, https://doi.org/10.5194/bg-19-5953-2022, 2022.

Schulzweida, U.: CDO User Guide, Zenodo, https://doi.org/10.5281/zenodo.10020800, version 2.3.0, 2023.

Schwarz, G.: Estimating the Dimension of a Model, Ann. Stat., 6, 461–464, https://doi.org/10.1214/aos/1176344136, 1978.

Singarayer, J. S., Valdes, P. J., Friedlingstein, P., Nelson, S., and Beerling, D. J.: Late Holocene methane rise caused by orbitally controlled increase in tropical sources, Nature, 470, 82–85, https://doi.org/10.1038/nature09739, 2011.

Sitch, S., Smith, B., Prentice, I. C., Arneth, A., Bondeau, A., Cramer, W., Kaplan, J. O., Levis, S., Lucht, W., Sykes, M. T., Thonicke, K., and Venevsky, S.: Evaluation of ecosystem dynamics, plant geography and terrestrial carbon cycling in the LPJ dynamic global vegetation model, Glob. Change Biol., 9, 161–185, https://doi.org/10.1046/j.1365-2486.2003.00569.x, 2003.

Skamarock, W. C. and Klemp, J. B.: A time-split nonhydrostatic atmospheric model for weather research and forecasting applications, J. Comput. Phys., 227, 3465–3485, https://doi.org/10.1016/j.jcp.2007.01.037, predicting weather, climate and extreme events, 2008.

Sweeney, C., Dlugokencky, E., Miller, C. E., Wofsy, S., Karion, A., Dinardo, S., Chang, R. Y.-W., Miller, J. B., Bruhwiler, L., Crotwell, A. M., Newberger, T., McKain, K., Stone, R. S., Wolter, S. E., Lang, P. E., and Tans, P.: No significant increase in long-term CH_4 emissions on North Slope of Alaska despite significant increase in air temperature, Geophys. Res. Lett., 43, 6604–6611, https://doi.org/10.1002/2016GL069292, 2016a.

Sweeney, C., Miller, J. B., Karion, A., Dinardo, S. J., and Miller, C. E.: CARVE: L2 Atmospheric Gas Concentrations, Airborne Flasks, Alaska, 2012–2015, https://doi.org/10.3334/ORNLDAAC/1404, accessed: 2026-06-17, 2016b.

Sweeney, C., McKain, K., Miller, B. R., and Michel, S. E.: ABoVE: Atmospheric Gas Concentrations from Airborne Flasks, Arctic-CAP, 2017, https://doi.org/10.3334/ORNLDAAC/1717, accessed: 2026-06-17, 2019.

Sweeney, C., Chatterjee, A., Wolter, S., McKain, K., Bogue, R., Conley, S., Newberger, T., Hu, L., Ott, L., Poulter, B., Schiferl, L., Weir, B., Zhang, Z., and Miller, C. E.: Using atmospheric trace gas vertical profiles to evaluate model fluxes: a case study of Arctic-CAP observations and GEOS simulations for the ABoVE domain, Atmos. Chem. Phys., 22, 6347–6364, https://doi.org/10.5194/acp-22-6347-2022, 2022.

Tan, Z. and Zhuang, Q.: Arctic lakes are continuous methane sources to the atmosphere under warming conditions, Environ. Res. Lett., 10, 054 016, https://doi.org/10.1088/1748-9326/10/5/054016, 2015.

Thompson, R. L., Sasakawa, M., Machida, T., Aalto, T., Worthy, D., Lavric, J. V., Lund Myhre, C., and Stohl, A.: Methane fluxes in the high northern latitudes for 2005–2013 estimated using a Bayesian atmospheric inversion, Atmos. Chem. Phys., 17, 3553–3572, https://doi.org/10.5194/acp-17-3553-2017, 2017.

Thornton, B. F., Wik, M., and Crill, P. M.: Double-counting challenges the accuracy of high-latitude methane inventories, Geophys. Res. Lett., 43, 12,569–12,577, https://doi.org/10.1002/2016GL071772, 2016.

Tian, H., Xu, X., Liu, M., Ren, W., Zhang, C., Chen, G., and Lu, C.: Spatial and temporal patterns of CH_4 and N_2O fluxes in terrestrial ecosystems of North America during 1979–2008: application of a global biogeochemistry model, Biogeosciences, 7, 2673–2694, https://doi.org/10.5194/bg-7-2673-2010, 2010.

https://doi.org/10.5194/egusphere-2026-6528
Preprint. Discussion started: 9 November 2026
© Author(s) 2026. CC BY 4.0 License.

van der Werf, G. R., Randerson, J. T., van Wees, D., Chen, Y., Giglio, L., Hall, J., Vernooij, R., Mu, M., Binte Shahid, S., Barsanti, K. C., Yokelson, R., and Morton, D. C.: Landscape fire emissions from the 5th version of the Global Fire Emissions Database (GFED5), Sci. Data, 12, 1870, https://doi.org/10.1038/s41597-025-06127-w, 2025.

Veraverbeke, S., Rogers, B. M., Goulden, M. L., Jandt, R. R., Miller, C. E., Wiggins, E. B., and Randerson, J. T.: Lightning as a major driver of recent large fire years in North American boreal forests, Nat. Clim. Change, 7, 529–534, https://doi.org/10.1038/nclimate3329, 2017.

Waigl, C. F., Stuefer, M., Prakash, A., and Ichoku, C.: Detecting high and low-intensity fires in Alaska using VIIRS I-band data: An improved operational approach for high latitudes, Remote Sens. Environ., 199, 389–400, https://doi.org/10.1016/j.rse.2017.07.003, 2017.

Wania, R., Ross, I., and Prentice, I. C.: Implementation and evaluation of a new methane model within a dynamic global vegetation model: LPJ-WHyMe v1.3.1, Geosci. Model Dev., 3, 565–584, https://doi.org/10.5194/gmd-3-565-2010, 2010.

Wania, R., Melton, J. R., Hodson, E. L., Poulter, B., Ringeval, B., Spahni, R., Bohn, T., Avis, C. A., Chen, G., Eliseev, A. V., Hopcroft, P. O., Riley, W. J., Subin, Z. M., Tian, H., van Bodegom, P. M., Kleinen, T., Yu, Z. C., Singarayer, J. S., Zürcher, S., Lettenmaier, D. P., Beerling, D. J., Denisov, S. N., Prigent, C., Papa, F., and Kaplan, J. O.: Present state of global wetland extent and wetland methane modelling: methodology of a model inter-comparison project (WETCHIMP), Geosci. Model Dev., 6, 617–641, https://doi.org/10.5194/gmd-6-617-2013, 2013.

Ward, R. H., Sweeney, C., Miller, J. B., Goeckede, M., Laurila, T., Hatakka, J., Ivakov, V., Sasakawa, M., Machida, T., Morimoto, S., Goto, D., and Ganesan, A. L.: Increasing methane emissions and widespread cold-season release from high-Arctic regions detected through atmospheric measurements, J. Geophys. Res.-Atmos., 129, e2024JD040 766, https://doi.org/10.1029/2024JD040766, e2024JD040766 2024JD040766, 2024.

Ward, R. H., Western, L. M., Tunnicliffe, R. L., Fillola, E., Tsuruta, A., Aalto, T., and Ganesan, A. L.: Uncertainty and retrieval sensitivity in TROPOMI-based methane inversions over the North Slope of Alaska, EGUsphere, 2025, 1–38, https://doi.org/10.5194/egusphere-2025-4230, 2025.

Watts, J. D., Ordway, E., Malone, S. L., Zhu, Q., Palmer, P. I., Patel-Tupper, D., Ciais, P., Li, F., Monteverde, D. R., Arndt, K. A., Bruhwiler, L., Buma, B., Cadillo-Quiroz, H., Euskirchen, E., Hoyt, A. M., Holgerson, M., Hugelius, G., Jackson, R. B., Jacob, D., Kuhn, M., Natali, S. M., Peng, S., Perryman, C. R., Poulter, B., Rey-Sánchez, C., Sagang, L. B., Schuur, E. A. G., Varner, R. K., and Vargas, R.: A global methane observation system to track climate feedbacks for verifiable climate impact, Science, 391, 1324–1327, https://doi.org/10.1126/science.aef0459, 2026.

Wittig, S., Berchet, A., Pison, I., Saunois, M., Thanwerdas, J., Martinez, A., Paris, J.-D., Machida, T., Sasakawa, M., Worthy, D. E. J., Lan, X., Thompson, R. L., Sollum, E., and Arshinov, M.: Estimating methane emissions in the Arctic nations using surface observations from 2008 to 2019, Atmos. Chem. Phys., 23, 6457–6485, https://doi.org/10.5194/acp-23-6457-2023, 2023.

Worthy, D. E. J., Levin, I., Trivett, N. B. A., Kuhlmann, A. J., Hopper, J. F., and Ernst, M. K.: Seven years of continuous methane observations at a remote boreal site in Ontario, Canada, J. Geophys. Res.-Atmos., 103, 15 995–16 007, https://doi.org/10.1029/98JD00925, 1998.

Ying, Q., Poulter, B., Watts, J. D., Arndt, K. A., Virkkala, A.-M., Bruhwiler, L., Oh, Y., Rogers, B. M., Natali, S. M., Sullivan, H., Armstrong, A., Ward, E. J., Schiferl, L. D., Elder, C. D., Peltola, O., Bartsch, A., Desai, A. R., Euskirchen, E., Göckede, M., Lehner, B., Nilsson, M. B., Peichl, M., Sonnentag, O., Tuittila, E.-S., Sachs, T., Kalhori, A., Ueyama, M., and Zhang, Z.: WetCH$_4$: a machine-learning-based upscaling of methane fluxes of northern wetlands during 2016–2022, Earth Syst. Sci. Data, 17, 2507–2534, https://doi.org/10.5194/essd-17-2507-2025, 2025.

Yuan, K., Li, F., McNicol, G., Chen, M., Hoyt, A., Knox, S., Riley, W. J., Jackson, R., and Zhu, Q.: Boreal–Arctic wetland methane emissions modulated by warming and vegetation activity, Nat. Clim. Change, 14, 282–288, https://doi.org/10.1038/s41558-024-01933-3, 2024.

https://doi.org/10.5194/egusphere-2026-6528
Preprint. Discussion started: 9 November 2026
© Author(s) 2026. CC BY 4.0 License.



Zhang, Z., Fluet-Chouinard, E., Jensen, K., McDonald, K., Hugelius, G., Gumbricht, T., Carroll, M., Prigent, C., Bartsch, A., and Poulter, B.: Development of the global dataset of Wetland Area and Dynamics for Methane Modeling (WAD2M), Earth Syst. Sci. Data, 13, 2001–2023, https://doi.org/10.5194/essd-13-2001-2021, 2021a.

Zhang, Z., Fluet-Chouinard, E., Jensen, K., McDonald, K., Hugelius, G., Gumbricht, T., Carroll, M., Prigent, C., Bartsch, A., and Poulter, B.: Development of the global dataset of Wetland Area and Dynamics for Methane Modeling (WAD2M), Earth Syst. Sci. Data, 13, 2001–2023, https://doi.org/10.5194/essd-13-2001-2021, 2021b.

Zhang, Z., Poulter, B., Melton, J. R., Riley, W. J., Allen, G. H., Beerling, D. J., Bousquet, P., Canadell, J. G., Fluet-Chouinard, E., Ciais, P., Gedney, N., Hopcroft, P. O., Ito, A., Jackson, R. B., Jain, A. K., Jensen, K., Joos, F., Kleinen, T., Knox, S. H., Li, T., Li, X., Liu, X., McDonald, K., McNicol, G., Miller, P. A., Müller, J., Patra, P. K., Peng, C., Peng, S., Qin, Z., Riggs, R. M., Saunois, M., Sun, Q., Tian, H., Xu, X., Yao, Y., Xi, Y., Zhang, W., Zhu, Q., Zhu, Q., and Zhuang, Q.: Ensemble estimates of global wetland methane emissions over 2000–2020, Biogeosciences, 22, 305–321, https://doi.org/10.5194/bg-22-305-2025, 2025.

Zhao, C., Andrews, A. E., Bianco, L., Eluszkiewicz, J., Hirsch, A., MacDonald, C., Nehrkorn, T., and Fischer, M. L.: Atmospheric inverse estimates of methane emissions from Central California, J. Geophys. Res.-Atmos., 114, https://doi.org/10.1029/2008JD011671, 2009.

Zhuang, Q., Guo, M., Melack, J. M., Lan, X., Tan, Z., Oh, Y., and Leung, L. R.: Current and future global lake methane emissions: A process-based modeling analysis, J. Geophys. Res.-Biogeo., 128, e2022JG007 137, https://doi.org/10.1029/2022JG007137, e2022JG007137 2022JG007137, 2023.

Zona, D., Gioli, B., Commane, R., Lindaas, J., Wofsy, S. C., Miller, C. E., Dinardo, S. J., Dengel, S., Sweeney, C., Karion, A., Chang, R. Y.-W., Henderson, J. M., Murphy, P. C., Goodrich, J. P., Moreaux, V., Liljedahl, A., Watts, J. D., Kimball, J. S., Lipson, D. A., and Oechel, W. C.: Cold season emissions dominate the Arctic tundra methane budget, P. Natl. Acad. Sci. USA, 113, 40–45, https://doi.org/10.1073/pnas.1516017113, 2016.

Zürcher, S., Spahni, R., Joos, F., Steinacher, M., and Fischer, H.: Impact of an abrupt cooling event on interglacial methane emissions in northern peatlands, Biogeosciences, 10, 1963–1981, https://doi.org/10.5194/bg-10-1963-2013, 2013.